Reaction route, mechanism, and procedure of the photoredox of U(Ⅵ) and Sb(Ⅲ) using a Fe 3 O 4 /TiO 2 /g-C 3 N 4 heterojunction nano- photocatalyst under visible sunlight

Chun Wang
Tianjin University
Han Jiao
Tianjin University
Yinbo Yang
Tianjin University
Lihong Wei
Shenyang Aerospace University
Ping Na (naping@tju.edu.cn)
Tianjin University

Research Article

Keywords: Fe3O4/TiO2/g-C3N4 heterojunction nano-photocatalyst , Photocatalytic oxidation-reduction , U(VI), Sb(III), Theoretical calculation

Posted Date: January 19th, 2023

DOI: https://doi.org/10.21203/rs.3.rs-2456964/v1

Abstract

Magnetic $Fe_3O_4/TiO_2/g\text{-}C_3N_4$, as a stable and recyclable ternary two-layer heterojunction nano-photocatalyst, has been synthesized to integrate the merits of each which can remove U( ) and Sb( ) through responding to almost full-wave band of visible of sunlight. Meanwhile through the combination of actual tests (free radical trapping tests), characterization (XRD, FT-IR, Raman, XPS, EXAFS and EPR) and theoretical calculations structure optimization, band structures, TDOS, electrostatic potential, charge density difference and Bader charge analysis) revealed reaction route, catalytic mechanism and reaction procedure of this photocatalytic reaction. It was found that the adsorption process took place between TiO_2/ $g\text{-}C_3N_4$ heterostructure in the form of $(C_3)–N–U( )–O_{2c}–Ti$ and $N…Sb( )–O_{2c}–Ti$ where $N_{(g\text{-}C3N4)}$ and $O_{(TiO\ 2)}$ played decisive roles. The built-in electric field and electronic structure motivated TiO_2 and $g\text{-}C_3N_4$ to accumulate a large amount of e^- to reduce U( ) and h^+ to oxidize Sb( ) respectively, and completed the light-induced redox reaction by making full use of the e^-, $^{\bullet}OH$ and $O_2^{\bullet}$ produced by photoexcited carriers which were difficult to recombine, finally, heterojunction complexes of $(C_3)–N–U( )–O_{2c}–Ti$, $C=N–U( )–O_{2c}–Ti$ and $N…Sb( )–O_{2c}–Ti$ were formed. Moreover, the two-way effect of $O_2^{\bullet}$ proved that the redox of U( ) and Sb( ) had a coupling relationship. In addition, $Fe_3O_4/TiO_2/g\text{-}C_3N_4$ prevented the damage of Fe_3O_4's photodissolution to its structure while Fe_3O_4 provided a new and interrelated path for the redox of U( ) and Sb( ).

1. Introduction

As a source of clean energy, nuclear power has attracted increasing attention [1]. Uranium, the main constituent of spent nuclear fuel, has been used more frequently, causing damage to healthy biological organisms through migration in groundwater or surface-water systems by numerous highly soluble hexavalent uranium ions (U( )) [2]. Simultaneously, the trivalent antimony, Sb( ), is an important pollutant in mine drainage [3] and the fission product of uranium [4] exhibits high toxicity and mobility. Therefore, it is important to develop new methods and mechanisms to effectively treat wastewater containing uranium and antimony.

Presently, there are a few reports on several methods to remove U( ), such as ion exchange [5], chemical reduction [6], and adsorption [7]. Sb( ) can be removed by adsorption [8], coagulation [3], and chemical oxidation [9]. The general route of chemical reduction and oxidation considered as a valid approach is to change U( ) [10] and Sb( ) [11] into low- or high-valence states with low toxicity and low mobility, which can easily be adsorbed.

Photocatalysis treatment technology has been widely studied for the remediation of polluted water, owing to its characteristics of using clean energy and mild reaction conditions [12, 13]. In the photocatalysis system, titanium dioxide (TiO_2) [14] and graphitic carbon nitride ($g\text{-}C_3N_4$) [15] are widely used as low-cost photocatalysts. The formation of a $TiO_2/g\text{-}C_3N_4$ heterostructure can improve their photocatalytic ability

by overcoming their limitations, including TiO_2's inability to respond to visible light and g-C_3N_4's high recombination of photogenerated electron–hole pairs [16]. Tong et al. and Ma et al. reported TiO_2/g-C_3N_4 nanosheets with enhanced photocatalytic activity toward the degradation of organic pollutants [17] and NO [18].

In principle, the photocatalytic reaction is a redox process. The valence band (VB) and conduction band (CB) positions of TiO_2 are approximately + 3.1 and − 0.1 V, respectively. Contrarily, g-C_3N_4 has a lower VB position and a more negative CB position; therefore, the special electronic structure of the heterojunction facilitates photogenerated electron and hole transfer directly between TiO_2 and g-C_3N_4 and separates them [19]. Therefore, we can use this heterojunction as a bridge to realize the coupling of uranium reduction and antimony oxidation, which enables a high removal rate. To the best of our knowledge, there are no reports on the simultaneous removal of U( ) and Sb( ) by photocatalysis technology.

Concomitantly, the photocatalysts are doped with Fe_3O_4 to endow them with high magnetism to improve the catalyst recovery and avert groundwater pollution [20, 21]. Additionally, because the photodissolution of Fe_3O_4 will affect the photocatalytic efficiency, it should be prevented from being sandwiched between the g-C_3N_4 and TiO_2 [22]. Therefore, Fe_3O_4/TiO_2/g-C_3N_4 with a two-layer heterojunction is designed to reduce environmental pollution while ensuring the stability of the material.

This study focuses on the preparation of highly efficient and magnetic catalysts that can couple uranium reduction and antimony oxidation and reveals the photocatalytic mechanism and changes in system structure with complex redox paths and competitive systems under the participation of photocarriers, free radicals, uranium, and antimony. The results showed that the magnetic heterojunction catalyst had great potential in wastewater treatment, thereby laying a foundation for the further development of highly efficient heterojunction photocatalyst materials that can simultaneously complete the oxidation and reduction of multiple pollutants.

2. Experimental

2.1. Synthesis of nanometer TiO_2

Three types of nanometer TiO_2 exposed {001}, {100}, and {101} facets via facile hydrothermal routes were synthesized here. According to the removal efficiency of them for U( ) and Sb( ), {001} facet TiO_2 exhibited best performance. Therefore, {001} facet TiO_2 was applied to the following study. The detailed synthesis methods and photocatalytic performance of three facet TiO_2 were exhibited in the Supporting Information (Text S1 and S2).

2.2. Synthesis of TiO_2/g-C_3N_4

6 g of urea was mixed with the as-prepared 0.25 g of {001}TiO_2, then the mixture was calcined under 550°C in a muffle furnace for 2 h at a heating rate of 8°C/min. After the reaction, the alumina crucible was cooled to room temperature, and the TiO_2/g-C_3N_4 with the yellow color was obtained, which abbreviated as TC. Basis of selecting for the optimum amount of urea were exhibited in the Text S3 and S4.

2.3. Synthesis of Fe_3O_4/TiO_2

In the synthesis of Fe_3O_4/TiO_2, acid-resistant Fe_3O_4 nanoparticles were adopted to decrease the incidence of Fe leaching during photocatalysis. A typical synthetic route was as follows [23]: 0.25 g of {001}TiO_2 was first transferred into a mixed solution containing KOH (4.05mL, 0.5 M), KNO_3 (4.05 mL, 2.0 M), and Milli-Q water (21.80 mL). After purged with N_2 for 1 h, a freshly prepared $FeSO_4$ solution(10.50 mL, 0.1 M) was added, followed by another 10 min N_2 purge. Finally, the reaction mixture was statically aged at 90°C for 2 h. The final black product was thoroughly washed by ethanol via magnetic separation and dried in vacuum at 50°C for 4 h. The abbreviation of Fe_3O_4/TiO_2 is FT. The optimization of Fe_3O_4 ratio in Fe_3O_4/TiO_2 could be found in the Text S5.

2.4. Synthesis of Fe_3O_4 /TiO_2/g-C_3N_4

30 mg of as-prepared TC and 30 mg of as-prepared FT powders were mixed in a solution containing Absolute Alcohol and Glycerin (3:1). After sonicated for 30 min, the as-prepared mixture was transferred into a Teflon-lined stainless steel autoclave, and then heated at 200°C in an oven for 24 h. The final black product was thoroughly washed by ethanol via magnetic separation and dried in vacuum at 50°C for 4 h. The abbreviation of Fe_3O_4/TiO_2/g-C_3N_4 is FTC. The details of best scale between FT and TC were mentioned in Text S6.

2.5. Simultaneous removal experiment of U(Ⅵ) and Sb(Ⅲ): Adsorption & Photocatalytic experiment

The stock solution with 20 ppm U( ) and 20 ppm Sb( ) was prepared by $UO_2(NO_3)_2$•$6H_2O$ (> 99.9% purity, MERYER) and $C_8H_4K_2O_{12}Sb_2$•$0.5H_2O$ (> 99.9% purity, MACKLIN) into 100 mL Milli-Q water. The pH values of the suspension were adjusted to 5.03 by adding a negligible volume of H_2SO_4 (0.1 M) or NaOH (0.1 M) solution.

During each experiment, 30 mg of FTC was suspended in the sealed colorimetric tube filled with the solution above mentioned. The solution was magnetically stirred in dark for 2 h to reach the adsorption-desorption equilibrium of U( ) and Sb( ) on the surface of photocatalyst. The colorimetric tube used a rubber plug, on which two disposable needles were inserted, one of which named No.1 was filled with the gas required, and the other named No.2 was empty.

Experiments were conducted in a box-type photoreactor with magnetic stirring cooled by circulation 20°C water. A 300 W Xe lamp (wavelength range 320 nm ≤ λ ≤ 780 nm, light intensity 160 mW/cm^2) was used

as the source of simulated sunlight. 5 mL aliquot of the solution were pipetted by No.2 needle in each 1 h and filtered through 0.45 μm nylon syringe filters after sealed the rubber plug in time, meanwhile injected 5 ml of gas with No.1 needle to maintain pressure balance. The pictures of photoreactor and colorimetric tube were in the Fig. S5.

The concentration of Sb( ) was analyzed by atomic fluorescence spectrophotometer [24]. And the concentration of U( ) was analyzed by UV–vis spectrometry with Arsenazo- as the chromogenic agent at wavelength of 652 nm[25, 26]. The concentration of iron was determined by ICP-OES.

All tests were performed for three times and results were averaged. Removal rate (%) of U( ) and Sb( ) by photocatalysts in solution were defined as Eq. (1)

$$\mathrm{removalrate}\,(\%) = \frac{C_t}{C_0}$$

1

where C_0 and C_t are the concentration (mg/L) of uranium and antimony at initial and contact time t (h), respectively. Removal rate (%) of U( ) and Sb( ) by photocatalysts during redox process were defined as Eq. (2)

$$\mathrm{reduction/oxidationremovalrate}\,(\%) = \frac{C_t}{C_{\mathrm{adsorbent}}}$$

2

where $C_{\mathrm{adsorbent}}$ is the concentration (mg/L) of uranium and antimony after being completely adsorbed.

2.6. Free radical capture

To further investigate the photocatalytic mechanism, free radicals species in the photocatalytic process were detected [27]. TBA (0.5 mM), EDTA-2Na (0.5 mM), BQ (0.5 mM), and $K_2Cr_2O_4$ (0.5 mM) were introduced as scavengers of hydroxyl radical ($^{\bullet}OH$), hole (h^+) superoxide radical ($O_2^{\bullet}$) and e^-, respectively [28]. In order to eliminate the influence of adsorption, all the above reagents were added after adsorption-desorption equilibrium. Other experimental steps were completely consistent with those in *2.5*. The photoreaction process was expressed by a first-order kinetic model after adsorption according to Eq. (3) [29]:

$$\ln\frac{c_t}{c_{\mathrm{adsorption}}} = -kt$$

3

where k is the first-order constant.

2.7. Recycling and Co-existing ions experiment

The stability of FTC was investigated through 7 cycles. After every cycle run, the photocatalysts were collected and washed by agitating magnetically for 6 h with Absolute Alcohol and Milli-Q water, respectively. Afterward, the photocatalysts were dried by in vacuum at 50°C for 4 h for the next cycle reaction. Because the condition of real water was complexity and the general cations (e.g., Na^+, K^+, Mg^{2+}, etc.) and anions (e.g., SO_{2-4}, CO_{2-3}, Cl^-, etc.) would influence the speciation and migration of the target metal ions [30–32], so the effects of co-existing ions were explored by 10 mM $NaNO_3$, KNO_3, $Mg(NO_3)_2$, Na_2CO_3, Na_2SO_4, and NaCl solution. The detailed methods were showed in the Text S7.

2.8. Material Characterization and Computational details

The material and reaction process were characterized and tested through SEM, TEM, XRD, FT-IR, Raman, UV-vis, EIS, Photocurrent measurements, the Mott–Schottky plots, VSM, XPS, PL, Zeta, ESR, and EXAFS. The detailed methods were showed in the Text S8 and the computational details were showed in the Text S9.

3. Results And Discussion

3.1. Material performance

The morphological structure of FTC was examined by SEM and TEM. Figure 1a shows spherical Fe_3O_4 nanoparticles, TiO_2 nanosheets with characteristics corresponding to the 001 facet [33], and rod-shaped g-C_3N_4 aggregated by many irregularly shaped sheets [34]. Fe_3O_4, TiO_2, and g-C_3N_4 coexisted in FTC, where Fe_3O_4 and g-C_3N_4 were accumulated on both sides of TiO_2, successively, in a noncontact manner. The area corresponding to Fe_3O_4/TiO_2 was observed in the front of the TEM image of FTC (Fig. 1b), which was dull and thick because of the sticking of Fe_3O_4 at the center of the sample. A rough area with TiO_2/g-C_3N_4 caused by the wrinkled sheets of g-C_3N_4 was observed behind Fe_3O_4/TiO_2. The Fe_3O_4/TiO_2 and TiO_2/g-C_3N_4 regions were extracted to obtain high-resolution (HR)-TEM images, where the lattice spacings of 0.24, 0.23, and 0.34 nm corresponded to TiO_2(001), Fe_3O_4(311), and g-C_3N_4(002), respectively. This confirmed that Fe_3O_4/TiO_2 and TiO_2/g-C_3N_4 connected by TiO_2 formed an entire nanometer FTC with a two-layer heterojunction. The models of FTC, TiO_2/g-C_3N_4, and Fe_3O_4/TiO_2 (Figs. 1b–c) intuitively described the structures of these materials.

Figure 1d shows the FT-IR spectra of the prepared materials. Compared with the known standard FT-IR spectrum, the absorption peaks of the prepared Fe_3O_4, TiO_2, and g-C_3N_4 could be attributed to the stretching vibration of the corresponding bond in the standard [35, 36]. One of the outstanding peak bands observed at 617 cm^{-1} in the pure Fe_3O_4 was the symmetric stretching of oxygen atoms along Fe–O–Fe bonds. This peak could not be found in FTC because of the overlap with the characteristic peak of the stretching vibrations of the Ti–O octahedron. The FT-IR results showed that the FTC heterojunction structure contained the undestroyed structures of Fe_3O_4, TiO_2, and g-C_3N_4.

Compared with the standard XRD patterns of the pure anatase phase (JCPDS No. 21-1272), Fe_3O_4 (JCPDS No. 01-1111), and g-C_3N_4 (JCPDS No. 50-1550), Fig. 1e shows that the corresponding characteristic peaks were observed in the FT, TC, and FTC nanocomposites. The positions of these peaks did not shift, indicating that the composition of these composites met the requirements. In addition, compared with the patterns of g-C_3N_4 and FT, the 37.8° and 27.4° peaks of TC were not evident probably because a large heterojunction formed between g-C_3N_4 and {001} TiO_2 restricted the stacking of g-C_3N_4 perpendicular to the (002) direction. The formation of the heterojunction also caused a series of peaks of Fe_3O_4 to be concealed in FT. Noteworthily, all the peaks in FT and TC were present in FTC, suggesting that FTC stably retained the ternary two-layer heterojunction with Fe_3O_4/TiO_2 and TiO_2/g-C_3N_4.

As shown in Fig. 1f, the structure of FTC was established by Fe_3O_4 [37], anatase TiO_2 [38], and g-C_3N_4 because all the peaks of FTC correlated with those in the Raman spectra of Fe_3O_4, TiO_2, and g-C_3N_4. The corresponding spectrum showed the following changes: the signals attributed to the Fe_3O_4 phase in FT were diminished, and the signals attributed to the g-C_3N_4 phase in TC became less intense and wide, suggesting a decrease in its crystallinity. These conversions attributed to the phonon confinement effect caused by the distortions led to the TiO_2 interaction with the Fe_3O_4 or g-C_3N_4 lattice. The FTC results showed that the peaks further shifted based on retaining the characteristic peaks of FT and TC, implying that electronic interaction occurred among the TiO_2 nanoparticles and Fe_3O_4 or g-C_3N_4 sheets. Thus, Fe_3O_4, g-C_3N_4, and TiO_2 were successfully coupled into a two-layer heterojunction.

The band-gap energies and absorption thresholds were calculated using the Tauc [39] plot approach after UV–VIS diffuse reflectance spectroscopy (Figs. 2a–b). The band-gap energies of the as-prepared Fe_3O_4, g-C_3N_4, and TiO_2 were 1.87, 2.80, and 3.20 eV, respectively, which correlated with reported results [40, 41]. According to the change trend of band-gap energies, the absorption intensity of FTC (675 nm) extended to UV–VIS light regions. The band-gap energies of FTC reduced to 1.96 eV after FT coupled with TC, which was mainly due to the addition of Fe_3O_4. Thus, the high photocatalytic activity of FTC was demonstrable by an almost full-wave band of visible sunlight.

FTC exhibited the highest intensity and fast photocurrent response, and the photocurrent slowly decreased (Fig. 2c). Fig. S6 shows the EIS results with a decreased electron-transfer resistance in FTC with the smallest diameter of the semicircular Nyquist plots. Thus, FTC exhibited more efficient charge separation. The transient photocurrent responses and EIS results of FTC and g-C_3N_4 were similar, showing that the heterojunction between g-C_3N_4 and TiO_2 had a more evident influence on photocatalytic performance. The flat-band potentials of g-C_3N_4 and TiO_2 shown in Mott–Schottky plots (Fig. 2d) correlated with reported results [40]. These plots, including the minimum slope belonging to FTC, exhibited positive slopes, indicating that they were all n-type semiconductors, and FTC exhibited the fastest charge-transfer rate. As shown in Fig. 2d, the flat-band potential (E_{FB}) of FTC was − 0.36 eV (*vs.* Ag/AgCl [42]), signifying the CB potential (E_{CB}) for FTC confirmed to be − 0.14 eV. Therefore, the corresponding VB potential (E_{VB}) of FTC was calculated as 1.82 eV using the band-gap energy (1.96 eV) (Fig. 2a). The E_{CB},

E_{VB} values of g-C_3N_4, TiO_2, and TC were calculated to be − 0.28, 2.52; −0.20, 3.00; and − 0.26 2.74 eV using the same method, respectively, indicating that the positions of g-C_3N_4 were lower than those of TiO_2. Therefore, electrons formed a space-charge layer when transferring in the CB from g-C_3N_4 to TiO_2. The amount of Fe_3O_4 (E_{CB} = − 0.04 eV, E_{VB} = 3.16 eV as reported) was relatively small, and the photoelectrochemical performance of Fe_3O_4/TiO_2 was poor. The follow-up adsorption model showed that the Fe_3O_4/TiO_2 heterojunction did not adsorb reactants. Therefore, the influence of Fe_3O_4 was not analyzed here.

3.1.2. Simultaneous removal experiment of U(⅄) and Sb(⅄)

Figures 3a–b show the changes in U( ) and Sb( ) with time or different materials. Figure 3b shows that there was no concentration change in U( ) and Sb( ) without FTC. Under simulated sunlight irradiation, the concentrations of U( ) and Sb( ) rapidly decreased in the solution over FTC after reaching an adsorption–desorption equilibrium. After 3 h of photocatalysis, approximately 93.0% of U( ) and 83.0% of Sb( ) were removed by FTC, which exhibited the best photocatalytic performance among TiO_2, g-C_3N_4, Fe_3O_4, FT, and TC (Fig. 3b). The normalized U L_{III}-edge EXAFS and Sb *K*-edge EXAFS spectra (Fig. 3c) could verify the photocatalytic effect of FTC, i.e., the valence states of U( ) and Sb( ) were maintained during the adsorption process. After the 3-h photocatalysis, the valence state of U( ) decreased close to + 4, while that of Sb( ) increased to approximately + 5. Figure 3b also shows that the removal rate of FTC for the solution with only U( ) was merely 70.8%, while it was just 63.9% for the pure Sb( ) solution; these rates were considerably lower than that for the mixed solution. The removal rate for the mixed solution was higher because the major active species for photocatalysis of U( ) and Sb( ) were reductive e^- and photooxidative groups (such as •OH), which competed for photogenerated electrons and holes, respectively [27], thereby fully harnessing the photocatalytic ability of FTC by preventing their recombination.

The magnetic property of these materials was characterized (Fig. 3d and Table S1). The saturation magnetic induction of FTC with a value of 16.02 emu/g was considerably higher than that of nonmagnetic TC. The coercive force of 116.75 Oe confirmed that FTC was a permanent magnet [43, 44] with stable magnetism and good dispersibility in the aqueous phase. Figure 3d shows that FTC could be easily separated using an external magnet and redispersed in the solution by slight shaking, which facilitated the recovery and reusability of the photocatalysts.

3.1.3. Recycling and Co-existing ions experiment

As shown in Fig. 4a, FTC could still maintain a relatively high removal rate for U( ) and Sb( ) after being recycled seven times. Although Fe_3O_4 was dissolved [22] after four cycles, the mass of photodissolution after seven cycles was still less than 4% of the mass of Fe_3O_4 in FTC. The barrier to the photodissolution of Fe_3O_4 was due to the effect of g-C_3N_4 with a low-lying CB, which hindered the transfer of photogenerated electrons in TiO_2 to Fe_3O_4. With an emergence of Fe^{3+} and Fe^{2+}, which could react with

U( ) [30, 45] and Sb( ) [46, 47], a new redox path was observed, leading to an increase in the removal rate after four cycles. The TEM and VSM results (Fig. 4d) showed that the morphology was maintained with a two-layer heterojunction, and there was practically no change in the magnetism of FTC after a seven-run cycle test and cleaning. Compared with those of Fe_3O_4, TiO_2, g-C_3N_4, and TC, the PL peak intensity of FTC was considerably less and just slightly changed after seven cycles (Fig. 4c), showing that FTC exhibited a low and stable recombination rate of photogenerated electrons and holes. These results confirmed that the properties of FTC were extremely stable. Furthermore, FTC could be used, as confirmed by the results shown in Fig. 4b, which indicated that the coexisting ions had only a minimal effect on the photocatalytic removal of U( ) and Sb( ) by FTC.

3.2. Reaction route

3.2.1. XPS analysis

For the XPS measurements (Fig. 5a), the peaks around 288, 399, 459, 531, 712, and 724 eV were attributed to the C 1s, N 1s, Ti 2p, O 1s, Fe $2p_{3/2}$, and Fe $2p_{1/2}$ photoelectrons. Notably, new peaks at 382 and 393 eV after adsorption and 380 and 391 eV after a 3-h photocatalysis were attributed to the U $4f_{7/2}$ and U $4f_{5/2}$ photoelectrons, respectively, indicating the successful adsorption and reaction of U( ) [48] on FTC. The spectra of O 1s and Sb 3d partly overlapped; therefore, the analysis of Sb( ) refers to the HR XPS spectra.

As shown in Fig. 5b, the HR O 1s spectrum exhibited two characteristic peaks at 530.0 and 531.5 eV, which could be assigned to the oxygen atoms in the lattice of TiO_2 or Fe_3O_4 and the $^{\bullet}OH$ group of FTC. It was further confirmed that the oxygen-containing functional groups contributed to the adsorption and photocatalysis of U( ) and Sb( ).

The HR XPS spectra of the N 1s (Fig. 5c) of FTC could be deconvoluted into three peaks at 398.7, 400.0, and 401.1 eV, which could be ascribed to C–N = C, N–(C_3), and C–N–H, respectively. The peak of N–(C_3) shifted to a low binding energy after adsorption till the end. The C–N = C bonds exhibited a similar change after the 3-h photocatalysis, which verified the stretching of bonds and a shift in the charge center. Therefore, preliminarily, it was assumed that N–(C_3) was the location where the adsorption occurred; C–N = C and N–(C_3) were regarded as the adsorption sites of the photocatalytic product.

It was concluded that the material exhibited excellent stability because the areas of all the peaks (including HR Ti 2p, C 1s, and Fe 2p XPS shown in Fig. S7) rarely changed after the reaction.

As shown in the HR U 4f XPS spectra (Fig. 5d), the peaks of U $4f_{5/2}$ and U $4f_{7/2}$ were deconvoluted into two components at 390.2 and 391.1 eV and 379.5 and 380.2 eV, respectively, where the peaks of 380.2 and 391.1 eV, instead of corresponding to U( ), belonged to UO_{2+x}, and the rest belonged to UO_2 [49, 50]. This confirmed that all the U( ) was practically reduced. Similarly, as shown in the HR XPS spectrum of Sb 3d (Fig. 5b), the peaks corresponding to Sb( ) at 529.9 and 539.8 eV after adsorption moved to 530.8

and 540.2 eV, respectively, corresponding to Sb( ) or Sb( ) [51] after a 3-h photocatalysis, confirming that all the Sb( ) was nearly oxidized.

3.2.2. EXAFS

To investigate the binding environment and short-range structure of Sb( ) and U( ) interacting in FTC, EXAFS spectroscopy was employed to confirm the sorption mechanism between them. Figures 6a and 6c show the k^3-weighted U L_{III}-edge Sb *K*-edge EXAFS spectra of the reference (UO2 + 2, UO_2, $Sb(OH)_3$, and $Sb(OH)_5$); adsorption; and after-3-h-of-photocatalysis samples, which exhibited a distinct cyclic evolution. The corresponding Fourier-transforms results are shown in Figs. 6b and 6d, and the corresponding parameters are tabulated in Table 1. The R-factor showed that this fitting work had high reliability.

Table 1
Structural parameters around U and Sb uranium for the reference and in the solution over FTC after adsorption and 3h photocatalysis derived from EXAFS analyses.

Sample	Path	N^a	R(Å)^b	σ^2(Å^2)^c	R factor
UO2 + 2	U-O_{ax}	2	1.75	0.0026	0.0058
	U-O_{eq}	5	2.51	0.0130	
UO_2	U-O	8	2.34	0.0086	0.0012
	U-U	12	3.65	0.0026	
	U-O_2	24	4.23	0.0013	
$Sb(OH)_3$	Sb-O	3	1.99	0.0039	0.0177
$Sb(OH)_5$	Sb-O	6	1.97	0.0037	0.0155
After adsorption	U-O_{ax}	2	1.82	0.0018	0.0184
	U-O_{eq}/O	6	2.23	0.0064	
	U-N	1	2.74	0.0038	
	Sb-O	3	2.04	0.0040	0.0164
After photocatalysis	U-O	2	2.11	0.0035	0.0131
	U-O_1	6	2.36	0.0069	
	U-N	2	2.63	0.0038	
	U-U	3	3.65	0.0065	
	U-O_2	14	4.23	0.0032	
	Sb-O	1	1.92	0.0030	0.0075
	Sb-O_1	5	2.02	0.0036	

[a] Coordination number.

[b] Distance between absorber and backscatter atoms.

[c] Debye-Waller factor to account for both thermal and structural disorders.

[d] Indicates the goodness of the fit.

As shown in Figs. 6a–b, for the typical structure of UO2 + 2, the spectral fitting led to O_{ax} (axial oxygen atom) at 1.75 Å and O_{eq} (equator oxygen atom) at 2.51 Å, which correlated with the distances reported for other uranyl aqueous species [52]. When U( ) was adsorbed in the middle of the TiO_2/g-C_3N_4 heterojunction by FTC, the aforementioned amplitudes were slightly stretched to 1.82 and 2.23 Å, respectively, and the other Fourier-transforms feature could be fitted by U–N with a bond distance of 2.74 Å. However, no new bond distance corresponding to that formed by the expected active-site formation of TiO_2 and U( ) after adsorption could be found in the results. Based on the change in coordination number, it was speculated that the active site of TiO_2 should be oxygen, which formed a coordination bond in the heterojunction whose length was similar to that of U = O bonds in UO2 + 2 and was listed with them. The formation of the heterojunction and coordination could also explain why the oscillation feature near 2.34 Å in the typical structure of UO_2 [53] changed to 2.11 and 2.36 Å after the 3-h photocatalysis. The coordination number of the U–N shell at 2.63 Å increased, suggesting that the nitrogen groups of g-C_3N_4 were more closely bound to U( ).

As shown in Figs. 6c–d, the change in the bond length of Sb( ) and its products after adsorption correlated with the aforementioned rule, i.e., squashing by the heterojunction altered the length Sb–O, compared with the standard bond length of the main species of Sb( ) ($Sb(OH)_3$) [54], and the bond formed by Sb( ) and active oxygen on TiO_2 was concealed in other Sb–O bonds. The fitting results of the samples tallied with those of the reference samples. Thus, it could be concluded that UO_2 and $Sb(OH)_5$ existed in the product.

Finally, the adsorption of U( ) and U( ) could be attributed to the inner-sphere surface complexation caused by $N_{(g-C\ 3N\ 4)}$–U, $O_{(TiO\ 2)}$–$U_{(UO2+\ 2)}$/$U_{(UO\ 2)}$, and $O_{(TiO\ 2)}$–$Sb_{(Sb(OH)\ 3)}$/$Sb_{(Sb(OH)\ 5)}$ within the TiO_2/g-C_3N_4 heterojunction.

3.2.3. DFT of structures

The results of previous material characterizations showed that the reaction site could be related to the TiO_2/g-C_3N_4 heterojunction. To confirm this, we optimized all the possible adsorption structures, including U( ) or Sb( ) adsorbed on one side of {001}TiO_2 or g-C_3N_4 and in the middle of the TiO_2/g-C_3N_4 and Fe_3O_4/TiO_2 heterojunction (previous experimental results showed that Fe_3O_4 hardly participated in the reaction; therefore, no relevant adsorption structures were established). The corresponding adsorption energies (Table S2) showed that the adsorption energies of UO2 + 2 and $Sb(OH)_3$ adsorbed within the TiO_2/g-C_3N_4 heterostructure were the lowest, which correlated with the previous conclusion that the TiO_2/g-C_3N_4 heterostructure was where the reaction occurred. The final adsorption models are shown in Figs. 7a and 7c. The models of the products in the heterojunctions after the reaction were optimized to determine the mechanism of photocatalysis (Figs. 7b and 7d). The removal rate in the solution over FTC was slightly higher than that over TC on the premise that no reaction occurred in the TiO_2/Fe_3O_4 heterojunction. This could be because the addition of Fe_3O_4 increased the dispersion of active sites on

TiO_2 [38]. The redox potentials of UO_2^{2+}/UO_2, $Sb(OH)_3/Sb(OH)_5$, and Fe( )/Fe( ) were 0.411, 0.59, and 0.77 V, respectively. Therefore, as mentioned in subsection 3.1.3, Fe_3O_4 could also participate in the reduction of U( ) and the oxidation of Sb( ) in an insoluble form, such that more U( ) and Sb( ) were removed. However, since these were not the main reactions, we do not discuss the TiO_2/Fe_3O_4 heterojunction in detail herein.

The length of the bonds related to U or Sb shown in these models correlated with the EXAFS results, which confirmed the authenticity of these models. Furthermore, the models reflected the changes in material structures, and the bonding environment correlated with the XPS results, thereby confirming that the unsaturated O_{2c} sites (Fig. S8) of {001}TiO_2 were regarded as some of the reaction sites that participated in the adsorption and photocatalytic reaction of U( ) and Sb( ). Based on this, N–(C_3) and C–N = C were the adsorption locations of U( ) and U( ), respectively, which were the products of the photoreduction reaction. The new bond formed after the reaction between U( ) and TiO_2/g-C_3N_4 strengthened the force between them, compared with that after adsorption. The corresponding adsorption energies (Table S2) showed that the adsorption energies of UO_2 + TiO_2/g-C_3N_4 and $Sb(OH)_5$+TiO_2/g-C_3N_4 were lower than those of UO2 + 2 + TiO_2/g-C_3N_4 and $Sb(OH)_3$+TiO_2/g-C_3N_4, respectively, which were conducive for the removal of U and Sb from the solution after the reaction.

The analysis results of the total density of states (TDOS) (Figs. 8a–b), projected density of states (PDOS) (Figs. 8c–d), and models (Fig. 7) after the adsorption and reaction jointly illustrated the formation of the new force. After adsorption, the new chemical bond originated from the U( ) 4f, Sb( ) 3s, and Sb( ) 3p orbitals hybridized with the O 2p, Ti 3d, and N 2p orbitals to form these heterojunction complexes, N–U( )–O–Ti and N…Sb( )–O–Ti. The photocatalytic product, UO_2, existed above the Fermi level in the energy range of 0.71–2.11eV because the electrons occupied the antibonding orbitals between UO_2 and the heterostructure. Through the analysis of the DOS redistribution caused by the exchange of electrons and the formation of new bonding displayed as s character states of Sb elevated to above the Fermi level of 2.9 eV, which hybridized with Ti, O, C, and N to form hybridization (Fig. 7d), we could infer that g-C_3N_4 used the accumulated holes to produce oxidized groups in the free space between it and $Sb(OH)_3$ and oxidized Sb( ) to create a strong interaction with g-C_3N_4 after the reaction. This phenomenon again clarified the role of g-C_3N_4 in Sb oxidation.

3.3. Catalytic mechanism

3.3.1. XPS analysis

As shown in Figs. 5b–c, after being optically excited, the peaks of O shifted to high binding energies, while the peaks of N slightly moved in the opposite direction, indicating that even if the photogenerated carriers were consumed by U( ) and Sb( ), the amount of e^- around O increased, while that around N reduced. It reflected the strong interface interaction between them and U and Sb. It was speculated that

photogenerated electrons and holes were detained on TiO_2 to reduce U( ) and g-C_3N_4 to oxidize Sb( ), respectively, after they were directed to transfer in TiO_2/g-C_3N_4.

3.3.2. DFT of Photocatalytic enhancement mechanism

The band structures, TDOS, and PDOS of the materials are shown in Figs. 9a and 9c. The calculated band gap of these materials was underestimated, compared with the experimental Eg because the actual materials had a certain thickness, while the models were single-layer structures. The DFT was limited in that the discontinuity in the exchange-correlation potential was not considered [55], but the trend of changes fitted with the experimental results and the calculated band gap of TiO_2 were similar to reported results [54, 56], which verified the rationality of the DOS. Figures 9a and 8c show that the N 2p, O 2p, and Ti 3d orbitals overlapped the 2π* antibonding orbitals near the Fermi level, confirming that there was a strong interaction among them, endowing FTC with high reactivity and a strong binding energy. Figure 9a shows that the CB maximum (CBM) of TiO_2/g-C_3N_4 was mainly occupied by the O and Ti atomic orbitals of TiO_2, and the N atomic orbital of g-C_3N_4 mostly controlled the VB maximum (VBM), which showed that FTC had a heterostructure and again determined the direction of charge separation and transfer, similar to the results of the Mott–Schottky plots and UV–VIS diffuse reflectance spectroscopy.

The calculated results of the charge-density difference (Fig. 9a) showed that charge redistribution occurred in the heterostructure. Bader charge analysis showed that a 0.03-eV charge transferred from g-C_3N_4 to TiO_2 on the other side of the heterojunction. The electrostatic potentials (Fig. S9) showed that g-C_3N_4 with a large work function (4.68 eV) was an oxidation-type photocatalyst, whereas TiO_2 (4.00 eV) was a reduction-type photocatalyst. When the electrons flowed from TiO_2 with a high Fermi level to g-C_3N_4 until the two Fermi energies reached the same level, the net charges distributed over both sides of the heterostructure formed a built-in electric field where negative and positive charges accumulated at g-C_3N_4 and TiO_2, respectively. Under illumination, since the CB edge potential of g-C_3N_4 was more negative than that of TiO_2, the photoinduced electrons on the g-C_3N_4 particle surfaces transferred easily to TiO_2, and the photoinduced holes on TiO_2 transferred to g-C_3N_4. The built-in electric field promoted the transfer of electrons from g-C_3N_4 to the CB of TiO_2 and hindered the photoexcited electrons in the CB of TiO_2 and holes generated in the VB of g-C_3N_4 from moving, which made them accumulate and difficult to compound. Oppositely, the recombination of photoexcited electrons and holes was more likely to occur in the VB of TiO_2 and CB of g-C_3N_4, but it prevented the holes and electrons in TiO_2 and g-C_3N_4, which had accumulated numerous electrons and holes, respectively, from being compounded by themselves.

From the charge-density difference after the adsorption and reaction (Figs. 9b–e), there was charge transfer among U( ), U( ), Sb( ), Sb( ), and TiO_2/g-C_3N_4. Further Bader charge analysis of the TiO_2/g-C_3N_4 + U model during the reaction showed that TiO_2 interacted with U and delivered 0.15 eV, whereas the electron shift obtained by g-C_3N_4 was 0.61 eV. With the same method used to analyze Sb, the two

aforementioned values became 0.25 and 0.04 eV, respectively, indicating that TiO_2 provided electrons for U during the photoreaction process. Contrarily, g-C_3N_4 contributed more to the oxidation of Sb, This correlated with the expected FTC performance and showed that the electrons accumulated on TiO_2 were fully utilized by U. In addition, the holes accumulated on g-C_3N_4 were fully utilized by Sb.

These results showed that the improvement in the photocatalytic ability of FTC was due to the enhancement of the separation of electrons and holes by the built-in electric field and the band structure through the regulation of the transmission path of photoexcited carriers. This process is intuitively shown in Fig. 10.

3.4. Reaction procedure: Photocatalytic enhancement mechanism

The sorption tendency of U( ) and Sb( ) on FTC accounted for the synergistic effect, including electrostatic interaction, surface complexation, and chemical precipitation. Sb( ) existed as uncharged $Sb(OH)_3$ over a wide pH range [54], suggesting that Sb( ) was tightly bound on the surface sites via the formation of surface complexes rather than electrostatic interaction. Zeta potential values (Fig. 11a) revealed that the point of zero charge (pH_{pzc}) of the surface was 5.03 mV. Electrostatic attraction between FTC and the positively charged UO_2^{2+} (the predominant U( ) species at low pH [57]) could be formed at pH > 5.03, which increased the pH_{pzc} to 5.42 mV after adsorption. The formation of electrically neutral UO_2, low-mobility Sb( ) species, or a negatively charged inner-sphere complex caused the pH_{pzc} to move toward a lower zeta potential after the reaction. Furthermore, using a pH of 5.03 for the solution ensured an accurate analysis of the mechanism of the photocatalytic reaction.

To study the possible active species generated during the photocatalytic processes, ESR analysis was performed (Figs. 11b–c). After 5 min of light irradiation, paramagnetic signals showed a 1:2:2:1 typical cleavage pattern of OH• and six characteristic peaks of the superoxide radical. The intensity of these peaks decreased after 3 h of photocatalysis. This result confirmed that $^{\bullet}OH$ and $O_2^{\bullet}$ were the main active species generated in the photocatalytic reaction. Considering that $^{\bullet}OH$ and $O_2^{\bullet}$ were produced by photogenerated holes, the photogenerated electrons on FTC were fully utilized.

To elucidate the mechanism of the photocatalytic reaction, free-radical trapping tests were performed over FTC. Figures 11d–f show the changes in the redox rates and concentrations of U( ) and Sb( ), and the first-order kinetic models are shown in Fig. S10. The reduction rate of U( ) was 87.9%, and the oxidation rate of Sb( ) was 73.2% without a scavenger.

For antimony (Figs. 11d–e), the scavenging of $O_2^{\bullet}$ and $^{\bullet}OH$ led to a decrease in the oxidation rate of Sb( ), indicating that they were both involved in the oxidation reaction. This conclusion correlated with that of the ESR experiment. EDTA-2Na, a scavenger of h^+, blocked the formation of $^{\bullet}OH$ [28], resulting in the poor oxidation of Sb( ). This was mutually verified by the results of trapping $^{\bullet}OH$ by TBA. Compared

with bubbling N_2 to discharge O_2 and prevent the generation of $O_2^{\bullet}$, the reaction speed and oxidation rate of Sb( ) after BQ scavenged $O_2^{\bullet}$ was higher, indicating that O_2 could directly participate in the oxidation of Sb( ) (Sb( ) + O_2→Sb( ) + $O_2^{\bullet}$). This could be verified by the fact that after $K_2Cr_2O_4$ consumed e^-, i.e., prevented O_2 from forming $O_2^{\bullet}$ with it [58], the oxidation rate of Sb( ) only dropped slightly and was considerably higher than that in the experiment of bubbling N_2. Moreover, the reduction rate and speed of Sb( ) increased after oxygen was added to the system to supplement O_2 and $O_2^{\bullet}$. Thus, $O_2^{\bullet}$, $^{\bullet}OH$, and O_2 jointly played important roles in the oxidation of Sb( ).

For uranium (Figs. 11d and f), the reduction rate of U( ) significantly dropped after $K_2Cr_2O_4$ consumed e^-, confirming that e^- was important for the reduction of U( ). Upon the addition of EDTA-2Na as an h^+ scavenger, the photogenerated electrons and holes were not easy to composite, and FTC provided more electrons for reduction. Therefore, it was again confirmed that e^- was significant for the reduction of U( ) through an increase in the uranium reduction rate and speed after h^+ was scavenged. The oxygen-free environment caused by N_2 and the absence of $O_2^{\bullet}$ caused by BQ reduced the reduction rate of U( ), which showed that $O_2^{\bullet}$ had a positive effect on the reduction of U( ) [59]. In addition, the reduction rate and speed of U( ) after adding BQ were lower than those under N_2. During the experiments filled with O_2 or N_2 (Figs. S10a and 11f), the reduction rate of the former slowed down, and the latter sped up. Based on these results and according to the premise that $O_2^{\bullet}$ was the product of O_2 and e^-, it could be inferred that the interaction principle between $O_2^{\bullet}$ and U( ) was as follows: O_2 competed with U( ) for photogenerated electrons to generate $O_2^{\bullet}$, which led to a reduction in speed; however, $O_2^{\bullet}$ could react with U( ) to generate low-valent uranium.

However, in theory, filling O_2 would lead to excessive O_2 competing for e^-, lowering the reduction rate of U( ) below that under N_2. However, the opposite was the reality. A relationship was made with the oxidation process of antimony, i.e., excessive O_2 oxidized antimony to generate $O_2^{\bullet}$ without competing for electrons, which reduced uranium. This conclusion that the $O_2^{\bullet}$ produced by the oxidation of Sb( ) and consumed by the reduction of U( ) was complementary could explain why ESR showed that the change in $^{\bullet}OH$ content during the reaction was more evident than that in the $O_2^{\bullet}$ content.

Summarily, the photocatalytic enhancement mechanism of FTC was to first use active substances, including $^{\bullet}OH$ and e^-, to compete for photogenerated electrons and holes, respectively, thereby fully harnessing the photocatalytic ability of FTC by preventing the recombination of the electrons and holes. The $O_2^{\bullet}$ generated by Sb( ) and O_2 to reduce U( )) and the consumption of $O_2^{\bullet}$ advanced the oxidation of Sb( ).

The reaction process was summarized as follows (4)-(15) and is shown in Fig. 12.

$$FTC + hv \rightarrow h^{+}_{VB}(g\text{-}C_3N_4) + e^{-}_{CB}(TiO_2) \quad (4)$$

$$UO_2^{2+} + 2\ e^{-}_{CB}(TiO_2) \rightarrow UO_2 \quad (5)$$

$$h^{+}_{VB}(g\text{-}C_3N_4) + H_2O \rightarrow H^{+} + {}^{\bullet}OH \quad (6)$$

$$Sb(OH)_3 + {}^{\bullet}OH \rightarrow Sb(OH)_4 \quad (7)$$

$$O_2 + e^{-}_{CB}(TiO_2) \rightarrow O_2^{\bullet -} \quad (8)$$

$$H_2O + Sb(OH)_4 + O_2 \rightarrow Sb(OH)_5 + O_2^{\bullet -} + H^{+} \quad (9)$$

$$2O_2^{\bullet -} + 2\ h^{+}_{VB}(g\text{-}C_3N_4) + 2H_2O \rightarrow 2H_2O_2 + O_2 \quad (10)$$

$$O_2^{\bullet -} + h^{+}_{VB}(g\text{-}C_3N_4) \rightarrow O_2 \quad (11)$$

$$2O_2^{\bullet -} + 2\ H^{+} \rightarrow 2H_2O_2 + O_2 \quad (12)$$

$$Sb(OH)_3 + H_2O_2 \rightarrow Sb(OH)_5 \quad (13)$$

$$O_2^{\bullet -} + UO_2^{2+} \rightarrow UO_2^{+} + O_2 \quad (14)$$

$$UO_2^{+} + e^{-}_{CB}(TiO_2) \rightarrow UO_2 \quad (15)$$

4. Conclusions

In this study, a $Fe_3O_4/TiO_2/g\text{-}C_3N_4$ ternary two-layer heterojunction nano-photocatalyst was synthesized whose removal rates of uranium and antimony under sunlight were 93.0% and 83.0%, respectively. $Fe_3O_4/TiO_2/g\text{-}C_3N_4$ harnessed the advantages of Fe_3O_4, TiO_2, and $g\text{-}C_3N_4$ in its magnetism and response to visible light and prevented the damage of Fe_3O_4's photodissolution to its structure. Ultimately, we fabricated a stable, recyclable, and efficient nano-photocatalyst material that can respond to an almost full-wave band of visible sunlight.

Theoretical calculations (structural optimization, band structures, and DOS) and characterizations (EXAFS spectroscopies) revealed the changes in the chemical bonds during the reaction. The structures of N–U( )–O–Ti and N…Sb( )–O–Ti were formed after adsorption, and new bonds were formed between N in C-N = C and the photocatalytic products. The O_{2c} in TiO_2 continuously played an important role in the formation of bonds. These conclusions confirmed the specific microstructural changes in the materials.

Other theoretical calculations (adsorption energy, electrostatic potential, charge-density difference, and Bader charge analysis) and characterizations (XPS) showed that the reaction occurred in the $TiO_2/g\text{-}C_3N_4$ heterojunction. The electronic structure of TiO_2 and $g\text{-}C_3N_4$ and the built-in electric field formed between them prevented the recombination of photogenerated carriers and promoted TiO_2 and $g\text{-}C_3N_4$ to separately accumulate numerous electrons and holes to reduce U( ) and oxidize Sb( ), respectively, which explains the high photocatalytic performance of $Fe_3O_4/TiO_2/g\text{-}C_3N_4$ during the photoreaction.

The free-radical trapping and ESR tests confirmed that in addition to the photogenerated electrons and holes, $O_2^{\bullet}$ and $^{\bullet}OH$ participated in the redox reaction. Among them, $O_2^{\bullet}$, an important bridge to connect the redox reaction, could be involved in the reduction of U( ) and the oxidation of Sb( ) in a two-way manner, confirming that the redox of U ( ) and Sb ( ) exhibited a coupling relationship. In addition, Fe_3O_4 provided a new and interrelated path for the redox of U( ) and Sb( ).

The prepared FTC harnessed the advantages and bypassed the disadvantages, clarified the division of different heterostructures, and exhibited a new coupling relationship between redox reactions. According to the exploration path of material performance → reaction route → catalytic mechanism → reaction procedure, this study completely explored the multiple interrelationships between a two-layer heterogeneous material and a series of reactions in which the material participated. This study provides a strategy for the construction of efficient photocatalysts for treating complex wastewater.

Abbreviations

FTC, $Fe_3O_4/TiO_2/g\text{-}C_3N_4$; SEM, scanning electron microscopy; TEM, transmission electron microscopy; CBM, conduction band maximum; VBM, valence band maximum; VSM, vibrating sample magnetometry; EIS, electrochemical impedance spectroscopy; XPS, X-ray photoelectron spectroscopy; EXAFS, extended X-ray absorption fine structure; ESR, electron-spin resonance.

Declarations

Funding

This study was funded by the 863 project (No. 2012AA063504), the National Natural Science Foundation of China (Nos. U1407116, 21276193), and the “National Key Research and Development Program of China” (No. 2020V2-0047).

Conflicts of interest/Competing interests

The authors have no conflicts of interest to declare that are relevant to the content of this article.

Contributions

Chun Wang wrote the main manuscript text, Han Jiao guided the characterization of materials, Yinbo Yang participated in DFT calculations, Lihong Wei provided the software needed for DFT calculations, and Ping Na gave the research direction of this study. All authors reviewed the manuscript.

Competing interests

The authors declare no competing interests.

References

1. Carrara, S (2020) Reactor ageing and phase-out policies: global and regional prospects for nuclear power generation. Energy Policy 147:111834. https://doi.org/ 10.1016/j.enpol.2020.111834.
2. Craft E, Abu-Qare A, Flaherty M, Garofolo M, Rincavage H, Abou-Donia M (2004) Depleted and natural uranium: chemistry and toxicological effects. J Toxicol Environ Health B Crit Rev 7:297-317. https://doi.org/10.1080/10937400490452714.
3. Guo X, Wu Z, He M (2009) Removal of antimony(V) and antimony(III) from drinking water by coagulation-flocculation-sedimentation (CFS). Water Res 3:4327-4335. https://doi.org/10.1016/j.watres.2009.06.033.
4. Carbol P, Solatie D, Erdmann N, Nylén T, Betti M (2003) Deposition and distribution of Chernobyl fallout fission products and actinides in a Russian soil profile. J Environ Radioact 68:27-46. https://doi.org/10.1016/S0265-931X(03)00027-4.
5. Heshmati H, Torab-Mostaedi M, Ghanadzadeh Gilani H, Heydari A (2014) Kinetic, isotherm, and thermodynamic investigations of uranium(VI) adsorption on synthesized ion-exchange chelating resin and prediction with an artificial neural network. Desalination Water Treat 55:1076-1087. https://doi.org/10.1080/19443994.2014.922495.
6. Zegke M, Nichol GS, Arnold PL, Love JB (2015) Catalytic one-electron reduction of uranyl(VI) to Group 1 uranyl(V) complexes via Al(III) coordination. ChemComm 51:5876-5879. https://doi.org/10.1039/C5CC00867K.
7. Han X, Wang Y, Cao X, Dai Y, Liu Y, Dong Z, Liu Y (2019) Adsorptive performance of ship-type nano-cage polyoxometalates for U(VI) in aqueous solution. Appl Surf Sci 484:1035-1040. https://doi.org/10.1016/j.apsusc.2019.04.121.
8. Wei D, Li B, Luo L, Zheng Y, Huang L, Zhang J, Huang H (2020) Simultaneous adsorption and oxidation of antimonite onto nano zero-valent iron sludge-based biochar: Indispensable role of reactive oxygen species and redox-active moieties. J Hazard Mater 391:122057. https://doi.org/10.1016/j.jhazmat.2020.122057.
9. Jiang W, Liu Y, Liu F, Li F, Shen C, Yang B, Sand W (2020) Ultra-fast detoxification of Sb(III) using a flow-through TiO_2-nanotubes-array-mesh based photoelectrochemical system. Chem Eng J 387:124155. https://doi.org/10.1016/j.cej.2020.124155.
10. Hua B, Deng B (2008) Reductive Immobilization of Uranium(VI) by Amorphous Iron Sulfide. Environ Sci Technol 42:8703-8708. https://doi.org/10.1021/es801225z.
11. Qi Z, Lan H, Joshi TP, Liu R, Liu H, Qu J (2016) Enhanced oxidative and adsorptive capability towards antimony by copper-doping into magnetite magnetic particles. RSC Adv 6:66990-67001. https://doi.org/10.1039/C6RA13412B.
12. Bai S, Gao C, Low J, Xiong Y (2019) Crystal phase engineering on photocatalytic materials for energy and environmental applications. Nano Res 12(9:2031-2054. https://doi.org/10.1007/s12274-018-2267-6.
13. Hu X, Kong L, He M (2014) Kinetics and mechanism of photopromoted oxidative dissolution of antimony trioxide. Environ Sci Techno 48:14266-14272. https://doi.org/10.1021/es503245v.

14. Sajan CP, Wageh S, Al-Ghamdi AA, Yu J, Cao S (2016) TiO_2 nanosheets with exposed {001} facets for photocatalytic applications. Nano Res 9:3-27. https://doi.org/ 10.1007/s12274-015-0919-3.
15. Hao Q, Jia G, Wei W, Vinu A, Wang Y, Arandiyan H, Ni B (2020) Graphitic carbon nitride with different dimensionalities for energy and environmental applications. Nano Res 13:18-37. https://doi.org/10.1007/s12274-019-2589-z.
16. Sridharan K, Jang E, Park TJ (2013) Novel visible light active graphitic C_3N_4–TiO_2 composite photocatalyst: Synergistic synthesis, growth and photocatalytic treatment of hazardous pollutants. Appl Catal B 142-143:718-728. https://doi.org/10.1016/j.apcatb.2013.05.077.
17. Tong Z, Yang D, Xiao T, Tian Y, Jiang Z (2015) Biomimetic fabrication of g-C_3N_4/TiO_2 nanosheets with enhanced photocatalytic activity toward organic pollutant degradation. Chem Eng J 260:117-125. https://doi.org/10.1016/j.cej.2014.08.072.
18. Ma J, Wang C, He H (2016) Enhanced photocatalytic oxidation of NO over g-C_3N_4-TiO_2 under UV and visible light. Appl Catal B 184:28-34. https://doi.org/10.1016/j.apcatb.2015.11.013.
19. Lin C, Liu B, Pu L, et al (2021) Photocatalytic oxidation removal of fluoride ion in wastewater by g-C_3N_4/TiO_2 under simulated visible light. Adv Compos Hybrid Mater 4:339–349. https://doi.org/10.1007/s42114-021-00228-x
20. Li ZJ, Huang ZW, Guo WL, Wang L, Zheng LR, Chai ZF, Shi WQ (2017) Enhanced Photocatalytic Removal of Uranium(VI) from Aqueous Solution by Magnetic TiO_2/Fe_3O_4 and Its Graphene Composite. Environ Sci Technol 51:5666-5674. https://doi.org/10.1021/acs.est.6b05313.
21. Peng Y, Luo L, Luo S, Peng K, Zhou Y, Mao QY, Zhou Q, Mao J, Yang Y (2021) Efficient Removal of Antimony(III) in Aqueous Phase by Nano-Fe_3O_4 Modified High-Iron Red Mud: Study on Its Performance and Mechanism. Water 13(6):809. https://doi.org/10.3390/w13060809.
22. Beydoun D, Amal R, Low GKC, McEvoy S (2000) Novel Photocatalyst: Titania-Coated Magnetite. Activity and Photodissolution. J Phys Chem B 104:4387-4396. https://doi.org/10.1021/jp992088c.
23. Sugimoto T, Matijević E (1980) Formation of uniform spherical magnetite particles by crystallization from ferrous hydroxide gels. J Colloid Interface Sci 74:227-243. https://doi.org/10.1016/0021-9797(80)90187-3.
24. El-Hadri F, Morales-Rubio A, de la Guardia M (2000) Atomic fluorescence spectrometric determination of trace amounts of arsenic and antimony in drinking water by continuous hydride generation. Talanta 52(4):653-662. https://doi.org/10.1016/S0039-9140(00)00400-8.
25. Savvin SB (1961) Analytical use of arsenazo III: Determination of thorium, zirconium, uranium and rare earth elements. Talanta 8:673-685. https://doi.org/10.1016/0039-9140(61)80164-1.
26. Rohwer H, Rheeder N, Hosten E (1997) Interactions of uranium and thorium with arsenazo III in an aqueous medium. Anal Chim Acta 341:263-268. https://doi.org/10.1016/S0003-2670(96)00559-4.
27. Pelaez M, Nolan NT, Pillai SC, Seery MK, Falaras P, Kontos AG, Dionysiou DD (2012) A review on the visible light active titanium dioxide photocatalysts for environmental applications. Appl Catal B 125:331-349. https://doi.org/10.1016/j.apcatb.2012.05.036.

28. Nosaka Y, Nosaka AY (2017) Generation and Detection of Reactive Oxygen Species in Photocatalysis. Chem Rev 117:11302-11336. https://doi.org/10.1021/acs.chemrev.7b00161.
29. Salomone VN, Meichtry JM, Litter MI (2015) Heterogeneous photocatalytic removal of U(VI) in the presence of formic acid: U(III) formation. Chem Eng J 270:28-35. https://doi.org/10.1016/j.cej.2015.01.118.
30. Zhang Y, Fein JB, Li Y, Yu Q, Zu B, Zheng C (2021) U(VI) adsorption to Fe_3O_4 nanoparticles coated with lignite humic acid: Experimental measurements and surface complexation modeling. Colloids Sur A Physicochem Eng Asp 614:126150. https://doi.org/10.1016/j.colsurfa.2021.126150.
31. Ren Y, Guo D, Zhao Z, Chen P, Li F, Yao J, Liu Y (2022) Singlet oxygen mediated photocatalytic Antimonite decontamination in water using nanoconfined TiO_2. Chem Eng J 435:134832. https://doi.org/10.1016/j.cej.2022.134832.
32. Hierro A, Martín JE, Olías M, Vaca F, Bolivar JP (2013) Uranium behaviour in an estuary polluted by mining and industrial effluents: The Ría of Huelva. Water Res 47:6269-6279. https://doi.org/10.1016/j.watres.2013.07.044.
33. Han X, Kuang Q, Jin M, Xie Z, Zheng L (2009) Synthesis of Titania Nanosheets with a High Percentage of Exposed (001) Facets and Related Photocatalytic Properties. J Am Chem Soc 131:3152-3153. https://doi.org/10.1021/ja8092373.
34. Huang ZA, Sun Q, Lv K, Zhang Z, Li M, Li B (2015) Effect of contact interface between TiO_2 and g-C_3N_4 on the photoreactivity of g-C_3N_4/TiO_2 photocatalyst: (001) vs (101) facets of TiO_2. Appl Catal B 164:420-427. https://doi.org/10.1016/j.apcatb.2014.09.043.
35. Pan J, Dong Z, Wang B, Jiang Z, Zhao C, Wang J, Li C (2019) The enhancement of photocatalytic hydrogen production via Ti^{3+} self-doping black TiO_2/g-C_3N_4 hollow core-shell nano-heterojunction. Appl Catal B 242:92-99. https://doi.org/10.1016/j.apcatb.2018.09.079.
36. Zhao M, Cui Z, Pan D, Fan F, Tang J, Hu Y, Wu W (2021) An Efficient Uranium Adsorption Magnetic Platform Based on Amidoxime-Functionalized Flower-like Fe_3O_4@TiO_2 Core–Shell Microspheres. ACS Appl Mater Interfaces 13:17931-17939. https://doi.org/10.1021/acsami.1c00556.
37. Guo H, Wang Y, Yao X, Zhang Y, Li Z, Pan S, Wang H (2021) A comprehensive insight into plasma-catalytic removal of antibiotic oxytetracycline based on graphene-TiO_2-Fe_3O_4 nanocomposites. Chem Eng J 425:130614. https://doi.org/10.1016/j.cej.2021.130614.
38. Challagulla S, Nagarjuna R, Ganesan R, Roy S (2016) Acrylate-based Polymerizable Sol–Gel Synthesis of Magnetically Recoverable TiO_2 Supported Fe_3O_4 for Cr(VI) Photoreduction in Aerobic Atmosphere. ACS Sustai Chem Eng 4:974-982. https://doi.org/10.1021/acssuschemeng.5b01055.
39. Zhang Y, Zhu M, Zhang S, Cai Y, Lv Z, Fang M, Wang X (2020) Highly efficient removal of U(VI) by the photoreduction of SnO_2/$CdCO_3$/CdS nanocomposite under visible light irradiation. Appl Catal B 279:119390. https://doi.org/10.1016/j.apcatb.2020.119390.
40. Jiang X, Xing Q, Luo X, Li F, Zou J, Liu S, Wang X (2018) Simultaneous photoreduction of Uranium(VI) and photooxidation of Arsenic(III) in aqueous solution over g-C_3N_4/TiO_2

heterostructured catalysts under simulated sunlight irradiation. Appl Catal B 228:29-38. https://doi.org/10.1016/j.apcatb.2018.01.062.

41. Chen M, Wu J, Lu C, Luo X, Huang Y, Jin B, Liang Z (2021) Photoreduction of CO_2 in the presence of CH_4 over g-C_3N_4 modified with TiO_2 nanoparticles at room temperature. Green Energy Environ 6:938-951. https://doi.org/10.1016/j.gee.2020.07.001.
42. Li Y, Wang R, Li H, Wei X, Feng J, Liu K, Zhou A (2015) Efficient and Stable Photoelectrochemical Seawater Splitting with TiO_2@g-C_3N_4 Nanorod Arrays Decorated by Co-Pi. J Phys Chem C 119:20283-20292. https://doi.org/10.1021/acs.jpcc.5b05427.
43. Jing J, Li J, Feng J, Li W, Yu WW (2013) Photodegradation of quinoline in water over magnetically separable Fe_3O_4/TiO_2 composite photocatalysts. Chem Eng J 219:355-360. https://doi.org/10.1016/j.cej.2012.12.058.
44. Sam SA, Balan AP, Kaipamangalath A, Varma MR, Nair RR, Thomas S (2021) Nanocomposite Permanent Magnets Based on $SrFe_{12}O_{19}$-Fe_3O_4 Hard-Soft Ferrites. J Supercond Nov Magn 34:3333-3344. https://doi.org/10.1007/s10948-021-06070-y.
45. Skomurski FN, Ilton ES, Engelhard MH, Arey BW, Rosso KM (2011) Heterogeneous reduction of U^{6+} by structural Fe^{2+} from theory and experiment. Geochim Cosmochim Acta 75:7277-7290. https://doi.org/10.1016/j.gca.2011.08.006.
46. Li W, Fu F, Ding Z, Tang B (2018) Zero valent iron as an electron transfer agent in a reaction system based on zero valent iron/magnetite nanocomposites for adsorption and oxidation of Sb(III). J Taiwan Inst Chem Eng 85:155-164. https://doi.org/10.1016/j.jtice.2018.01.032.
47. Zhang T, Chen J, Xiong H, Yuan Z, Zhu Y, Hu B (2021) Constructing new Fe_3O_4@MnOx with 3D hollow structure for efficient recovery of uranium from simulated seawater. Chemosphere 283:131241. https://doi.org/10.1016/j.chemosphere.2021.131241.
48. Gong X, Tang L, Zou J, Guo Z, Li Y, Lei J, He R (2022) Introduction of cation vacancies and iron doping into TiO_2 enabling efficient uranium photoreduction. J Hazard Mater 423:126935. https://doi.org/10.1016/j.jhazmat.2021.126935.
49. Al Rayyes AH, Ronneau C (1991) X-Ray Photoelectron Spectroscopy of Cesium Uranates. Radiochim Acta 54:189-192. https://doi.org/10.1524/ract.1991.54.4.189.
50. Winer K, Colmenares CA, Smith RL, Wooten F (1987) Interaction of water vapor with clean and oxygen-covered uranium surfaces. Surf Sci 183:67-99. https://doi.org/10.1016/S0039-6028(87)80336-9.
51. Li X, Qian J, Xu J, Sun Y, Liu L (2019) Synthesis and electrical properties of antimony-doped tin oxide-coated TiO_2 by polymeric precursor method. Mater Sci Semicond Process 98:70-76. https://doi.org/10.1016/j.mssp.2019.03.024.
52. Niu Z, Wei X, Qiang S, Wu H, Pan D, Wu W, Fan Q (2019) Spectroscopic studies on U(VI) incorporation into $CaCO_3$: Effects of aging time and U(VI) concentration. Chemosphere 220:1100-1107. https://doi.org/10.1016/j.chemosphere.2019.01.010.

53. O'Loughlin EJ, Kelly SD, Cook RE, Csencsits R, Kemner KM (2003) Reduction of uranium(VI) by mixed iron(II)/iron(III) hydroxide (green rust): formation of UO_2 nanoparticles. Environ Sci Technol 37:721-727. https://doi.org/10.1021/es0208409.
54. Yan L, Song J, Chan T, Jing C (2017) Insights into Antimony Adsorption on {001} TiO_2: XAFS and DFT Study. Environ Sci Technol 51:6335-6341. https://doi.org/10.1021/acs.est.7b00807.
55. Perron H, Roques J, Domain C, Drot R, Simoni E, Catalette H (2008) Theoretical investigation of the uranyl ion sorption on the rutile TiO_2(110) face. Inorg Chem 47:10991-10997. https://doi.org/10.1021/ic801246k.
56. Zhao Z, Liu Q (2008) Designed Highly Effective Photocatalyst of Anatase TiO_2 Codoped with Nitrogen and Vanadium Under Visible-light Irradiation Using First-principles. Catal Letters 124:111-117. https://doi.org/10.1007/s10562-008-9433-5.
57. Selli E, Eliet V, Spini MR, Bidoglio G (2000) Effects of Humic Acids on the Photoinduced Reduction of U(VI) in the Presence of Semiconducting TiO_2 Particles. Chem Eng J 34:3742-3748. https://doi.org/10.1021/es991319q.
58. Wahlström E, Vestergaard EK, Schaub R, Rønnau A, Vestergaard M, Lægsgaard E, Besenbacher F (2004) Electron Transfer-Induced Dynamics of Oxygen Molecules on the TiO_2(110) Surface. Science 303:511-513. https://doi.org/10.1126/science.1093425.
59. Li P, Wang Y, Wang J, Dong L, Zhang W, Lu Z, Fan Q (2021) Carboxyl groups on g-C_3N_4 for boosting the photocatalytic U(VI) reduction in the presence of carbonates TiO_2. Chem Eng J 414:128810. https://doi.org/10.1016/j.cej.2021.128810.

Figures

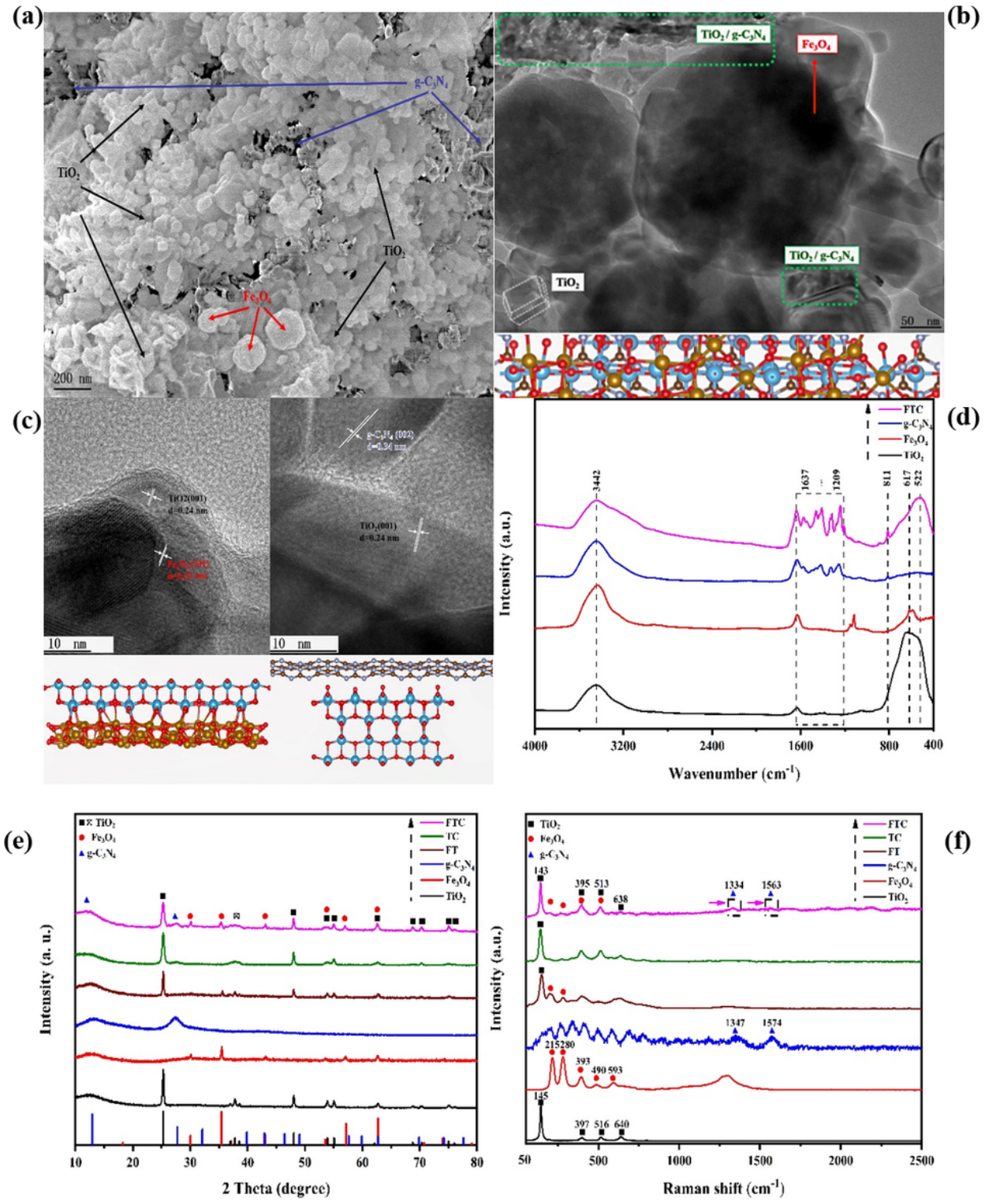

Figure 1

SEM image of nanometer FTC (a); TEM image and model of nanometer FTC (b); HR-TEM images and models of nanometer FTC (c); FT-IR spectra of TiO_2, Fe_3O_4, g-C_3N_4 and FTC (d); XRD patterns (e) and Raman spectra (e) of TiO_2, Fe_3O_4, g-C_3N_4, FT, TC, and FTC.

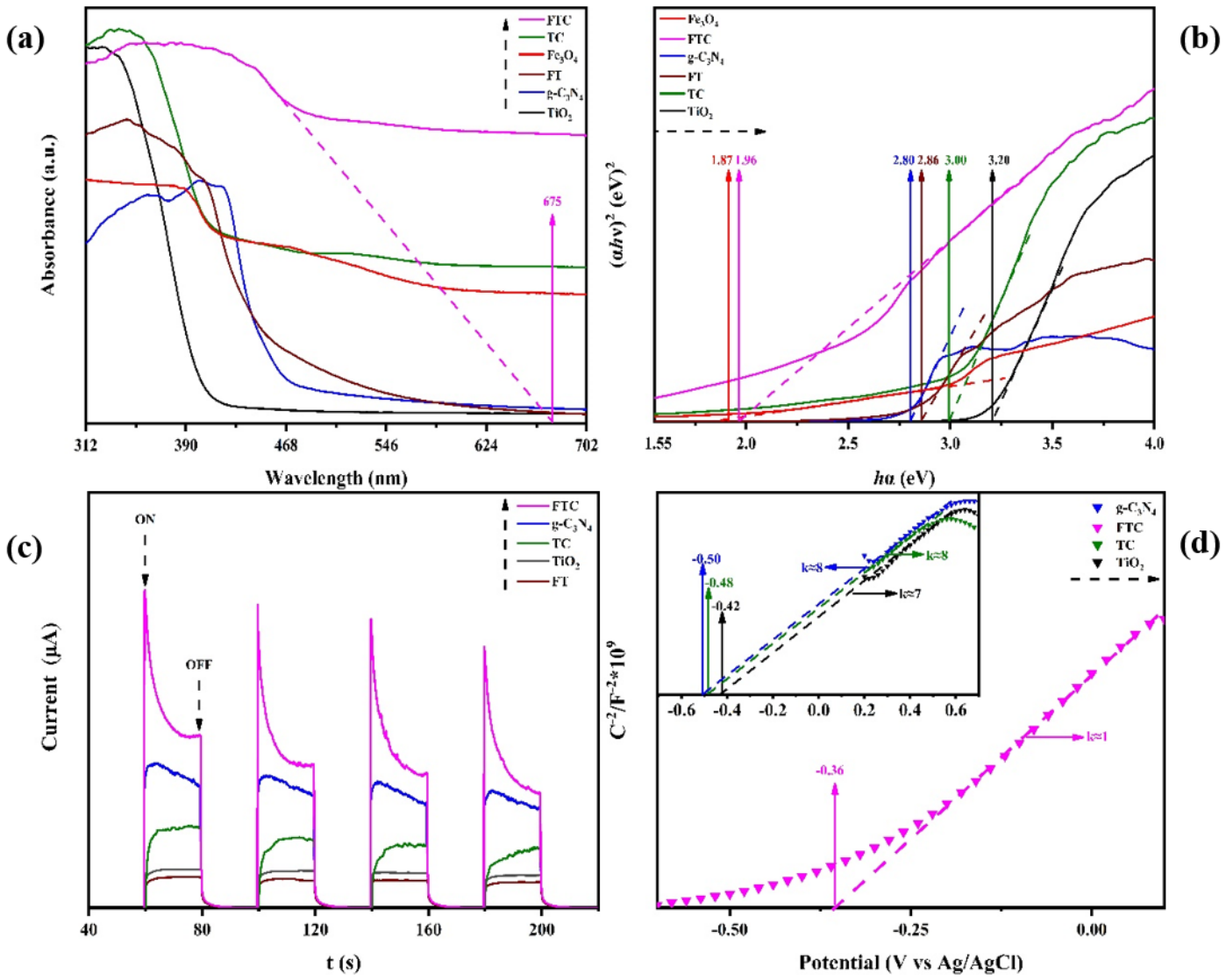

Figure 2

UV–visible diffuse reflection of TiO_2, Fe_3O_4, g-C_3N_4, FT, TC, and FTC (a) and calculated by Tauc plot (b); Transient photocurrent response of TiO_2, g-C_3N_4, FT, TC, and FTC (c); Mott-Schottky plots of TiO_2, g-C_3N_4, TC, and FTC (d).

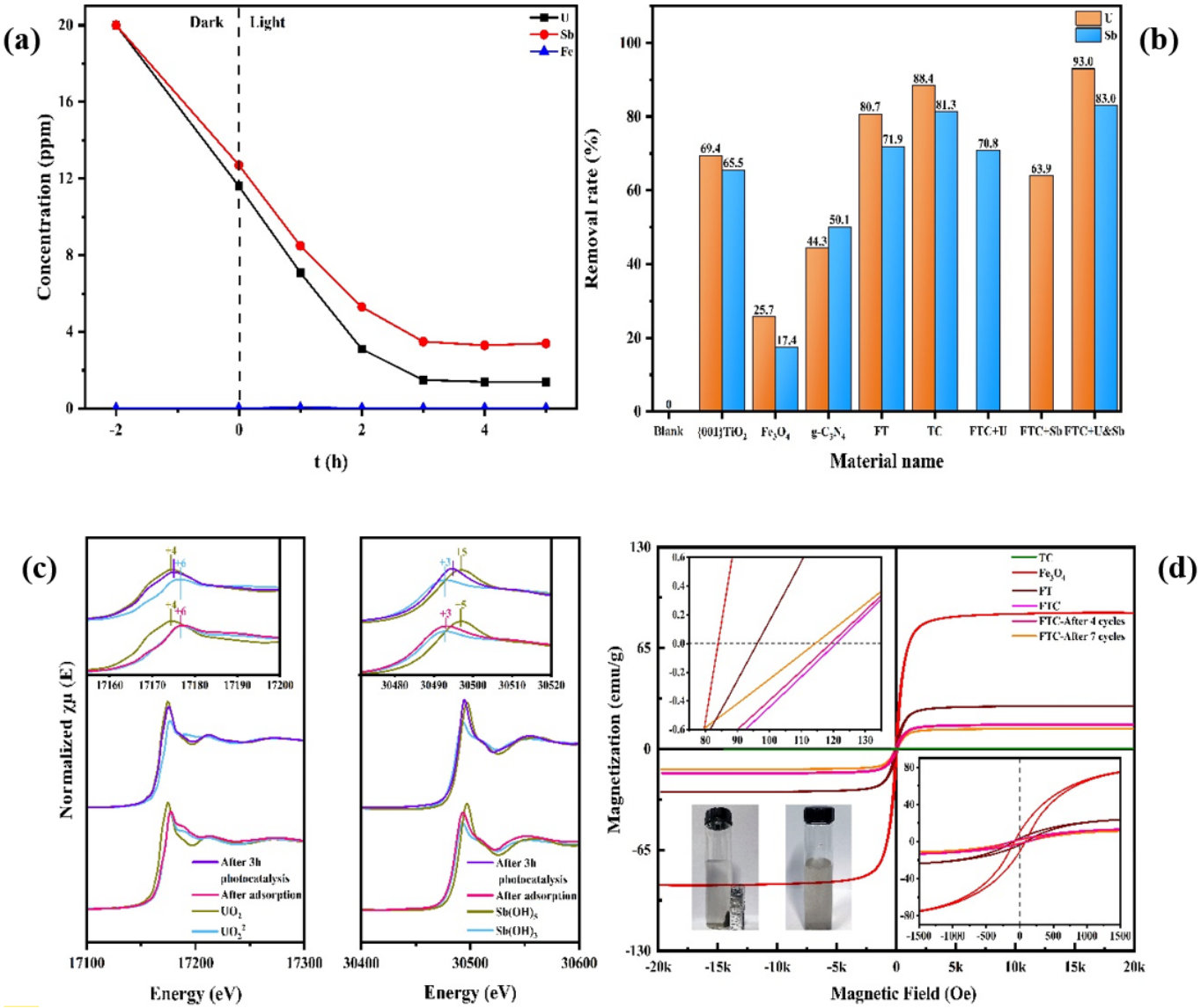

Figure 3

Concentration of U( ), Sb( ) and Fe in the solution over FTC (a); Removal rate of U( ) and Sb( ) by different materials (b); Normalized U L_{III}-edge EXAFS and Sb *K*-edge EXAFS spectra after adsorption and 3h photocatalysis (c); Magnetic property of Fe_3O_4, FT, TC, FTC before and after cycles (d).

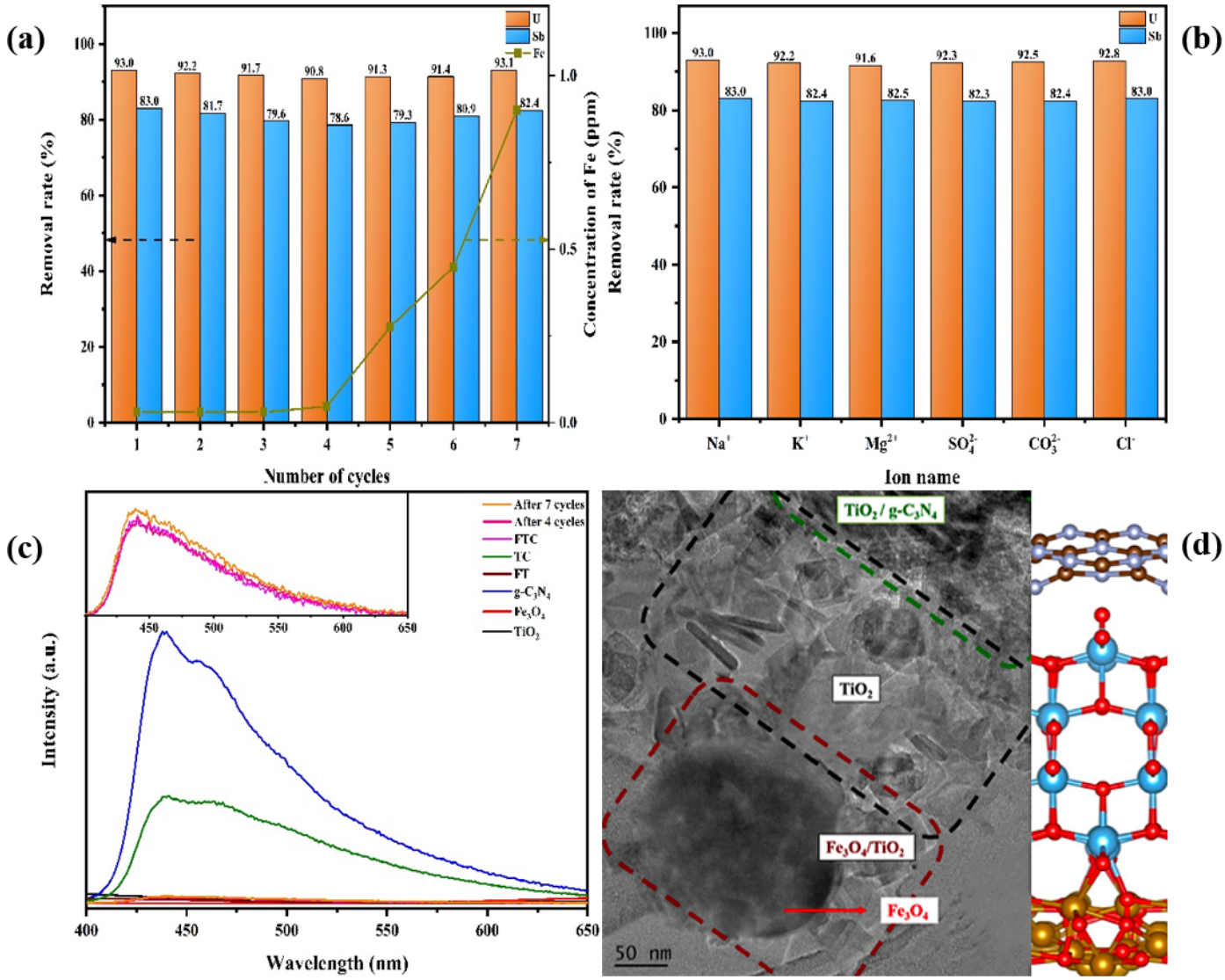

Figure 4

Removal of U( ), Sb( ) and Fe in the solution over FTC after cycling runs (a) and with co-existing ions (b); PL of TiO_2, Fe_3O_4, g-C_3N_4, FT, TC, FTC, FTC after 4 cycles and after 7 cycles (c); TEM and model of FTC after 7 cycles (d).

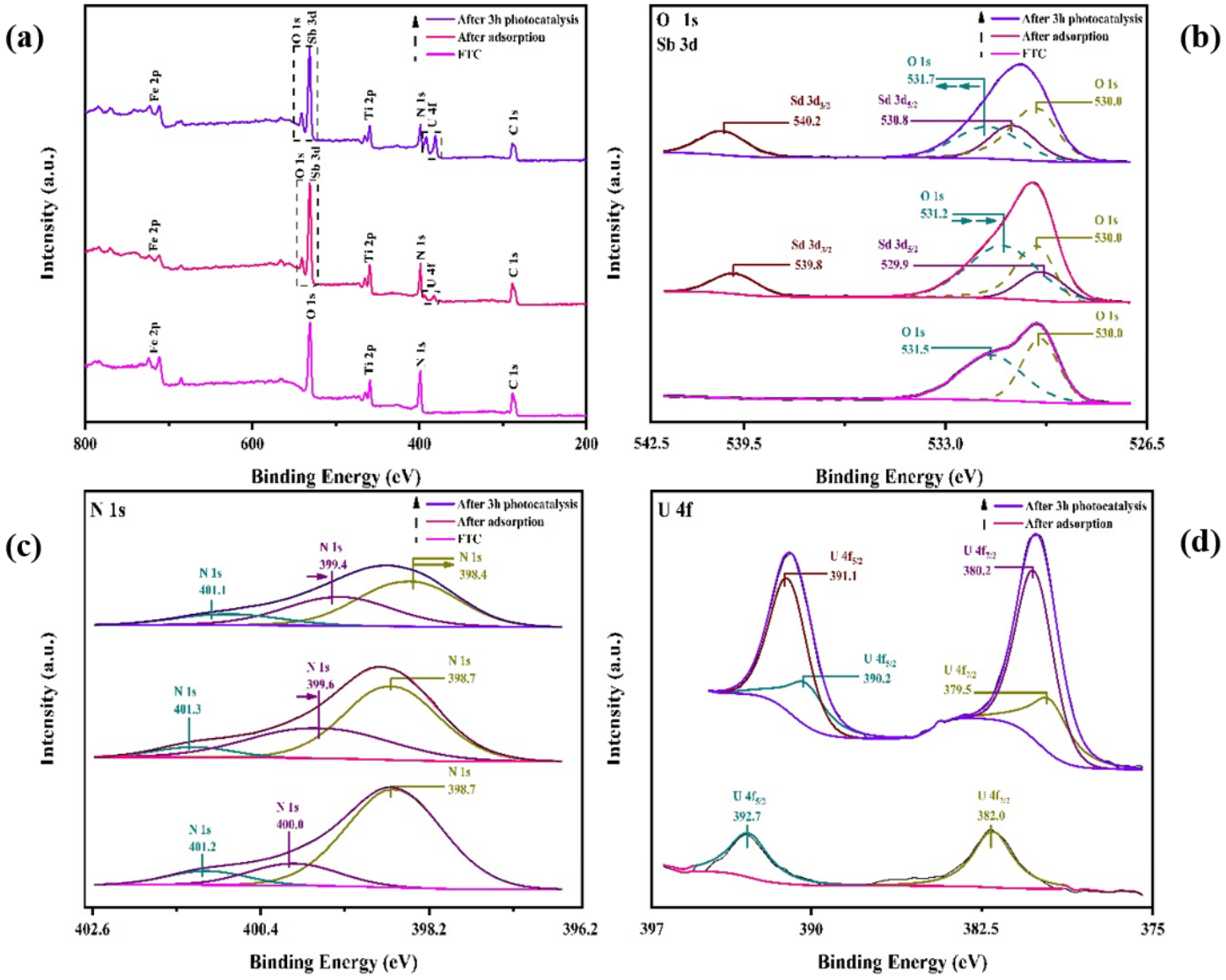

Figure 5

XPS spectra of survey (a), high-resolution O 1s (b) and high-resolution N 1s (c) of FTC after adsorption and 3h photocatalysis; XPS spectra of high-resolution Sb 3d (b) and high-resolution U 4f (d) in the solution over FTC after adsorption and 3h photocatalysis.

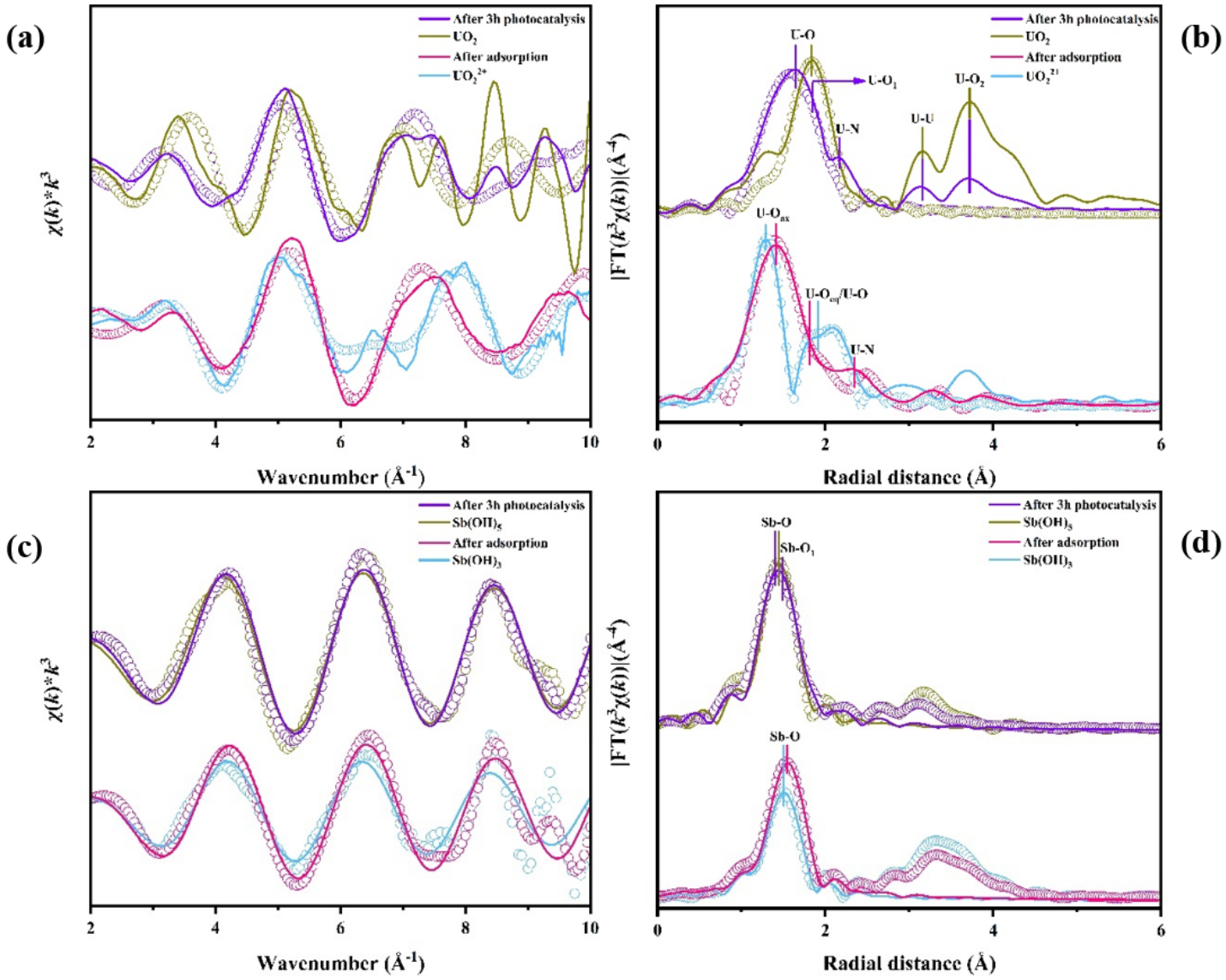

Figure 6

k^3-weighted U L_{III}edge EXAFS spectra (a) and corresponding Fourier-transforms results (b) for the reference and in the solution over FTC after adsorption and 3h photocatalysis; k^3-weighted Sb *K*-edge EXAFS spectra (c) and corresponding Fourier-transforms results (d) for the reference and in the solution over FTC after adsorption and 3h photocatalysis.

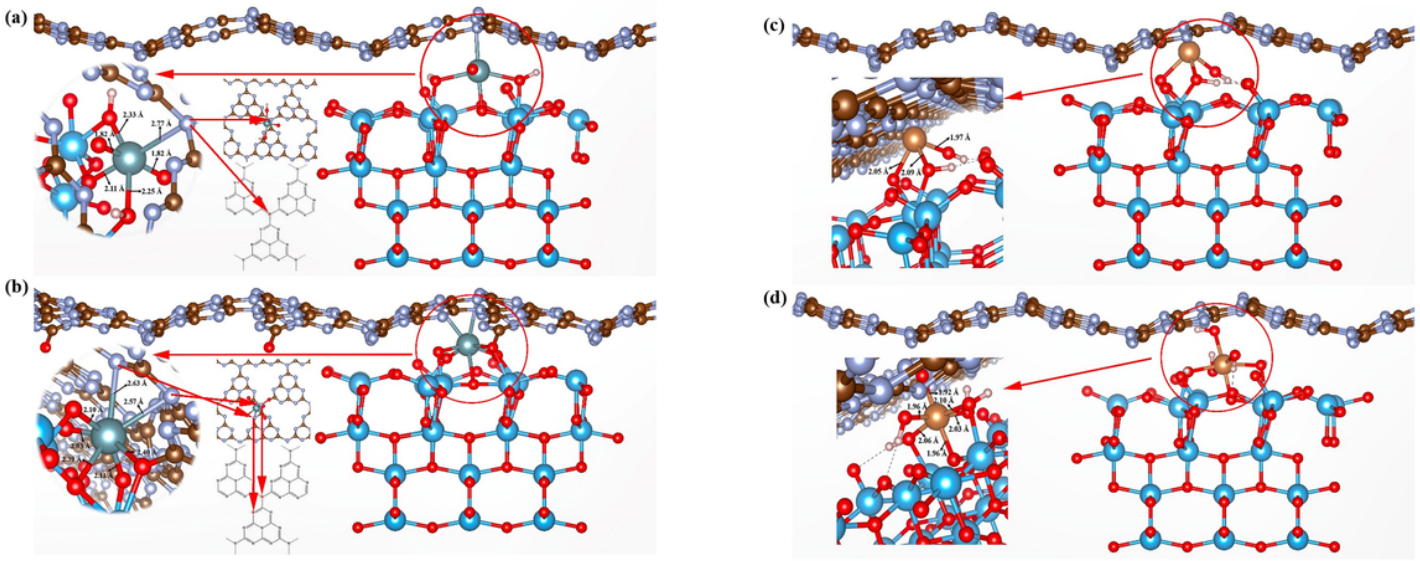

Figure 7

Adsorption model of TiO_2/g-C_3N_4+U( ) (a); Adsorption model of TiO_2/g-C_3N_4+U( ) (b); Adsorption model of TiO_2/g-C_3N_4+Sb( ) (c); Adsorption model of TiO_2/g-C_3N_4+Sb( ) (d).

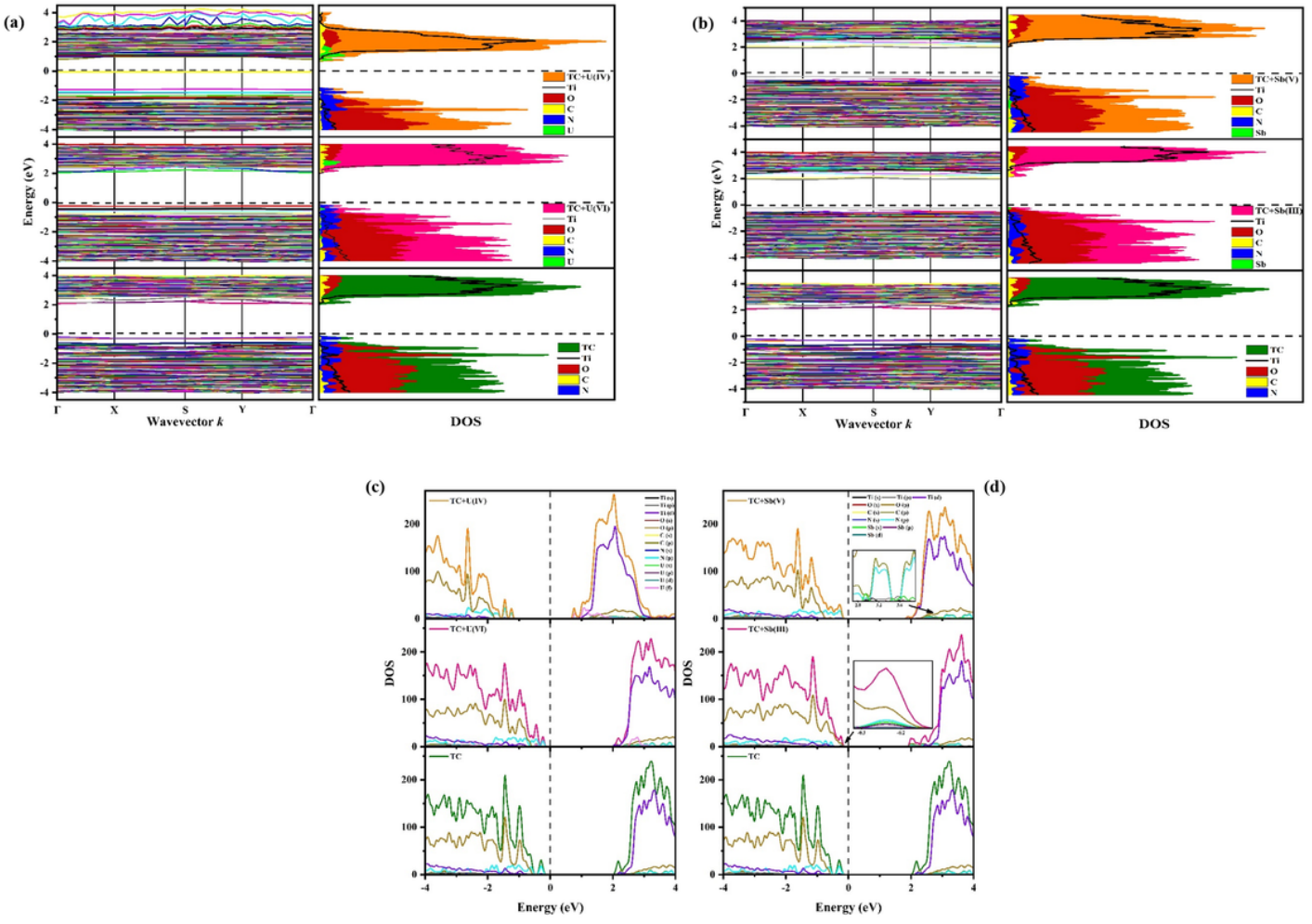

Figure 8

Band structures and TDOS of TiO_2/g-C_3N_4, TiO_2/g-C_3N_4+U( ), and TiO_2/g-C_3N_4+U( ) (a); Band structures and TDOS of TiO_2/g-C_3N_4, TiO_2/g-C_3N_4+ Sb( ), and TiO_2/g-C_3N_4+ Sb( ) (b); PDOS of TiO_2/g-C_3N_4, TiO_2/g-C_3N_4+U( ), and TiO_2/g-C_3N_4+U( ) (c); PDOS of TiO_2/g-C_3N_4, TiO_2/g-C_3N_4+ Sb( ), and TiO_2/g-C_3N_4+ Sb( ) (d).

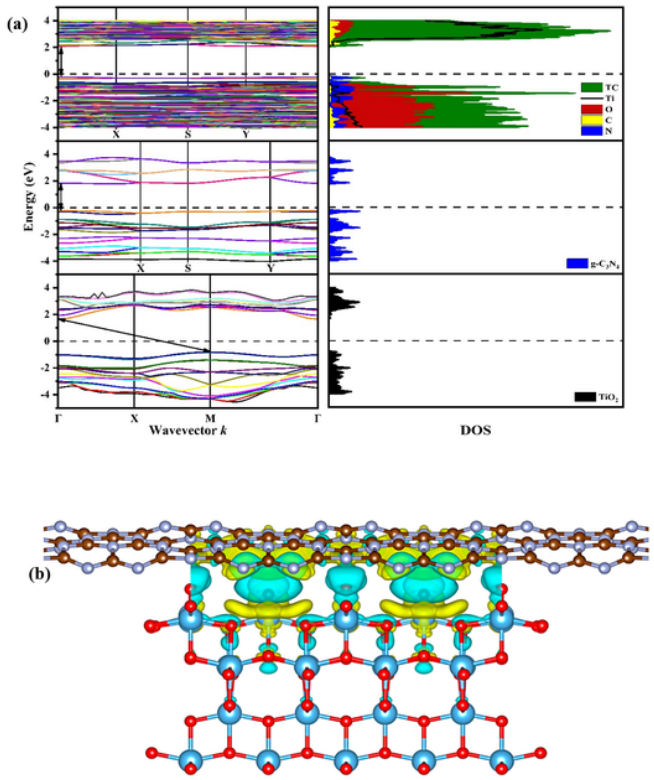

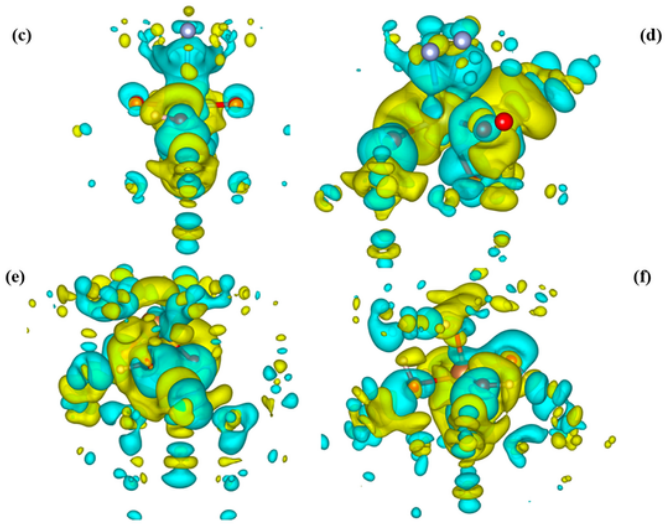

Figure 9

Band structures and TDOS of TiO_2, g-C_3N_4, and TiO_2/g-C_3N_4 (a); Charge density difference of TiO_2/g-C_3N_4 (b), TiO_2/g-C_3N_4+U( ) (c), TiO_2/g-C_3N_4+U( ) (d), TiO_2/g-C_3N_4+ Sb( ) (e), and TiO_2/g-C_3N_4+ Sb( ) (f). (The yellow and blue bubbles represented negative and positive charges, respectively.)

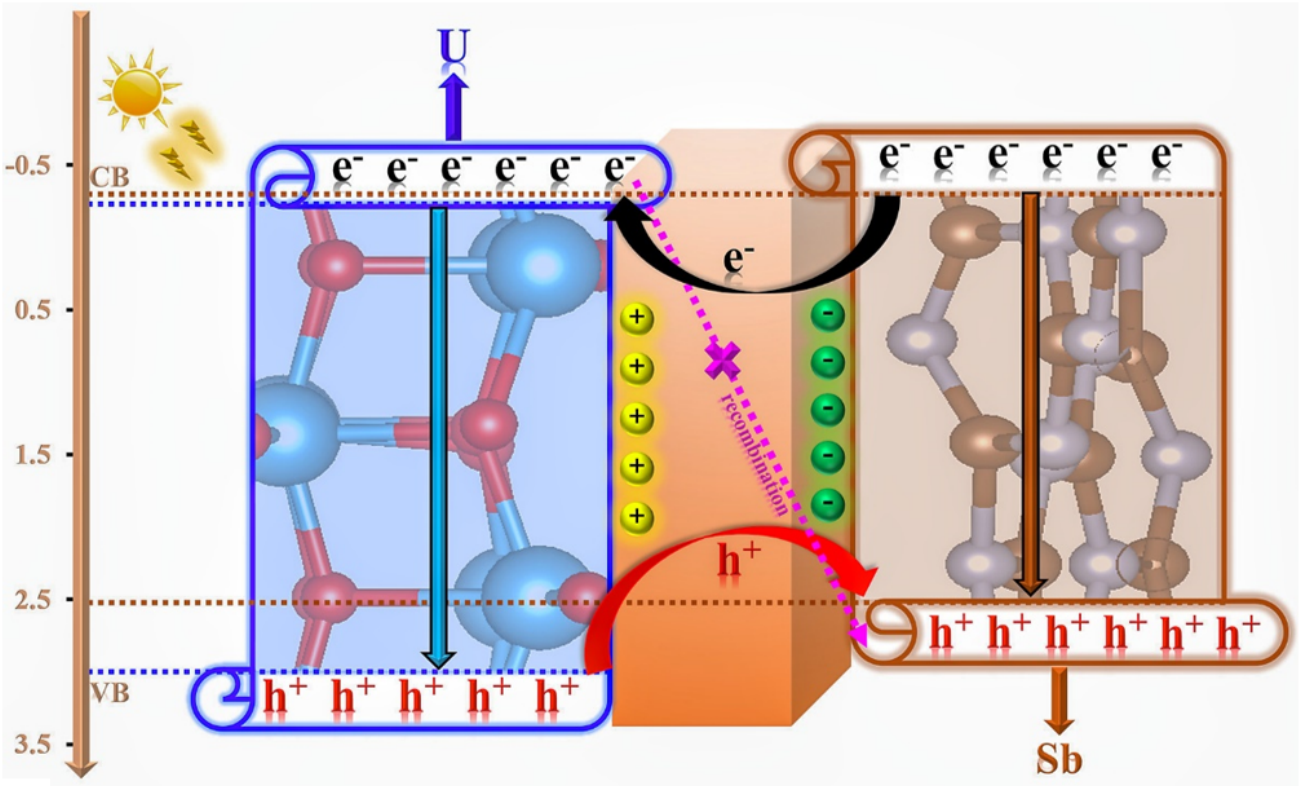

Figure 10

Built-in electric field and the transmission path of photoexcited carriers.

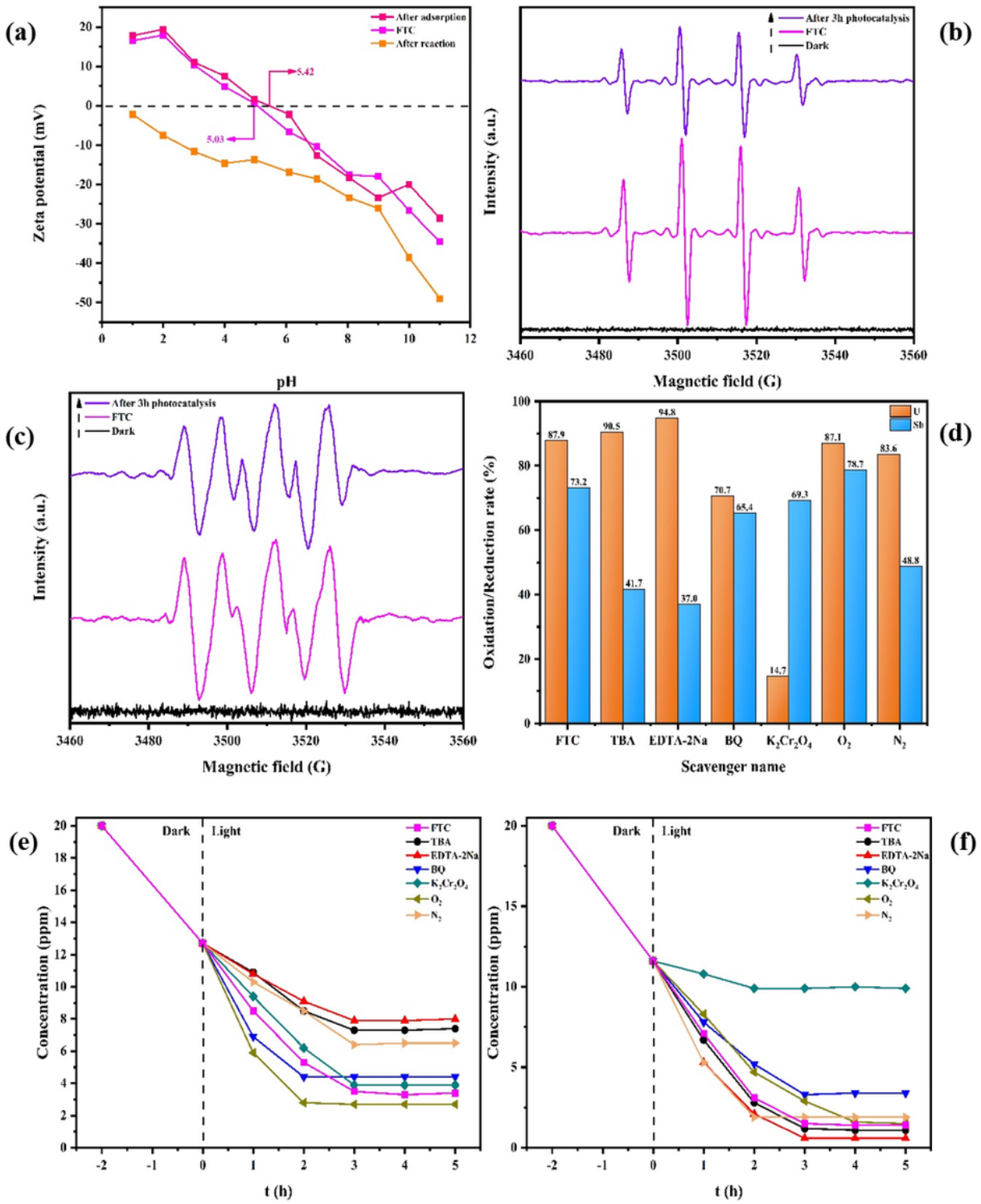

Figure 11

Zeta potential of the FTC, FTC after adsorption and FTC after reaction (a); ESR spectra of DMPO-$^{\cdot}$OH adducts over FTC and FTC after 3 h photocatalysis (b); ESR spectra of DMPO-$O_2^{\cdot}$ adducts over FTC and FTC after 3 h photocatalysis (c); Reduction of U( ) and Oxidation of Sb( ) in the solution over FTC with different scavengers (d); Influence of various scavengers on the concentration of Sb( ) in the solution over FTC (e); Influence of various scavengers on the concentration of U( ) in the solution over FTC (f).

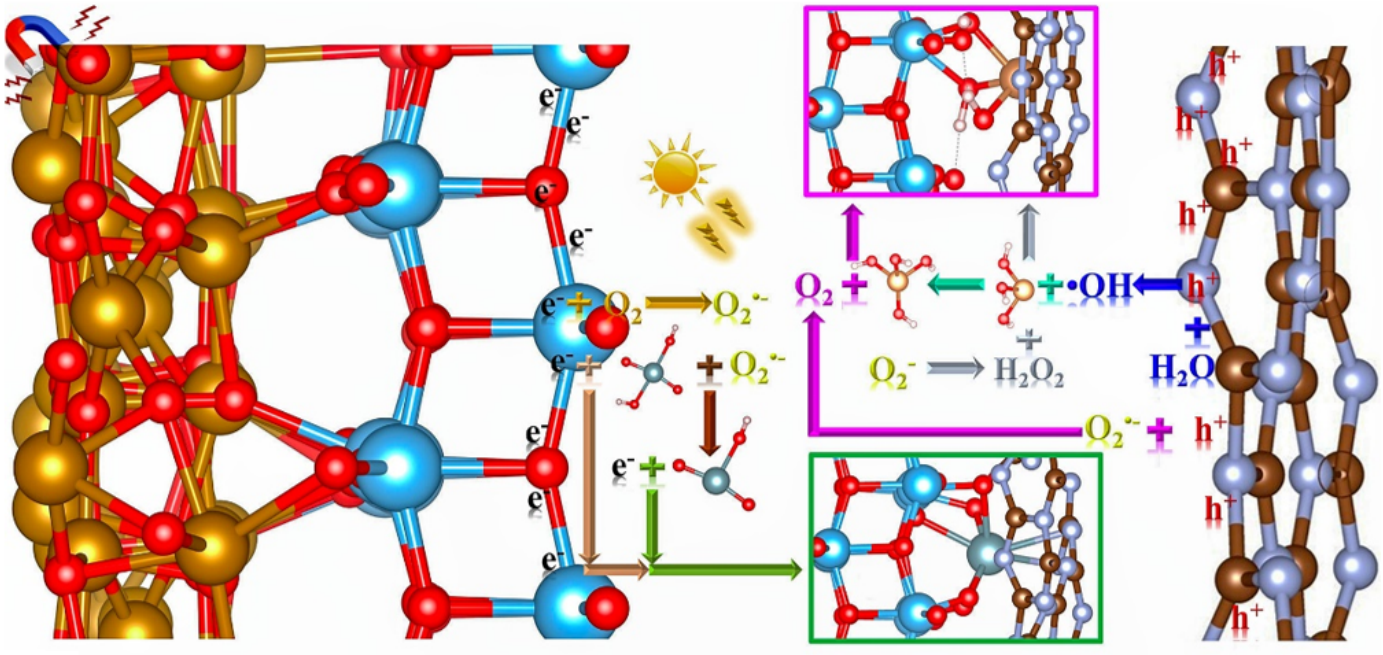

Figure 12

The reaction process of reducing U( ) and oxidizing Sb( ) in the solution over FTC.

Supplementary Files

This is a list of supplementary files associated with this preprint. Click to download.

- SIAdvComposHybridMater.docx